2023-08

Satellite-based shoreline detection along high-energy macrotidal coasts and influence of beach state

Konstantinou, A

10.1016/j.margeo.2023.107082
Marine Geology
Elsevier BV

Marine Geology 462 (2023) 107082

Contents lists available at ScienceDirect

Marine Geology

journal homepage: www.elsevier.com/locate/margo

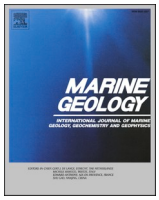

Invited research article

Satellite-based shoreline detection along high-energy macrotidal coasts and influence of beach state

Aikaterini Konstantinou [a,*], Tim Scott [a], Gerd Masselink [a], Kit Stokes [a], Daniel Conley [a], Bruno Castelle [b]

[a] Coastal Processes Research Group, School of Biological and Marine Sciences, University of Plymouth, Plymouth PL4 8AA, UK
[b] University of Bordeaux, CNRS, Bordeaux INP, EPOC, UMR 5805, F-33600 Pessac, France

ARTICLE INFO

Editor: Edward Anthony

Keywords:
Satellite shoreline detection
Shoreline change
Wave runup
Remote sensing
Beach state
CoastSat

ABSTRACT

Earth observation coupled with novel image analysis techniques now present a unique and powerful tool for the historical study of shoreline change at local to global scale. However, satellite-derived shoreline (SDS) data is limited in certain areas and is associated with large uncertainties relating to environmental factors, tidal range, and wave action. We use 14 years of monthly topographic surveys at two macrotidal sites in the UK representing end members of beach type (reflective, dissipative) to investigate the influence of tidal elevation and wave action on SDS accuracy. We find that applying appropriate water level corrections can significantly improve SDS accuracy. Results show that a different approach is required for water level definition depending on beach type and reveal that ultimately SDS accuracy is primarily controlled by beach state (beach profile shape). Accounting for tidal elevation led to substantial accuracy improvement at both sites and formed the optimal SDS strategy for the reflective site (Slapton). At the dissipative site (Perranporth) considering wave-induced water level fluctuations (wave setup and/or runup), including wave shoaling, was critical for reducing the tidally corrected SDS RMSE by a third and the mean bias by three quarters. An important realization for areas with high cloud cover such as the UK, and/or low satellite coverage, was that critically low image availability restricts temporally the type of phenomenon that can be detected (e.g., seasonal/interannual variability) and may compromise computed long-term trends. Our results suggest that the optimal approach is site-specific and depends on the shoreline translation method used and is therefore different depending on the application. We propose optimal SDS strategies to increase confidence in SDS extraction in meso-macrotidal environments with potentially low satellite useability (i.e., high cloud cover and/or low satellite coverage) depending on the spatial scale of the intended application. Long-term trends derived using this approach can reproduce trends from ground-based surveys and therefore enable more accurate projections of future shoreline position to be made.

1. Introduction

Understanding the rate and trajectory of geomorphological change of sedimentary coastlines is a fundamental requirement for effective coastal management and policy making (e.g., Boak and Turner, 2005; Nicholls et al., 2007; Burningham and French, 2017). However, changes along the shoreline occur over a wide range of timescales and vary significantly temporally and spatially. Intense storm events can result in extreme morphological change within hours on localized scales (e.g., Harley et al., 2017; Anfuso et al., 2020), whilst sea level rise drives coastal evolution at millennial timescales (Allen, 2000; Clemmensen et al., 2012). In between, decadal-scale cycles of shoreline change have often been reported (Brooks and Spencer, 2014; Turner et al., 2016; Hein et al., 2019). Importantly, although storm-driven shoreline changes can be significant in the short-term (Harley et al., 2022), future shoreline modelling indicates that the longer, decadal-scale component can often dominate long-term shoreline change (Vitousek et al., 2017; Wiggins et al., 2020; McCarroll et al., 2021). Interannual and decadal timescales are of particular interest as they are primarily driven by changes in incident wave conditions (Dodet et al., 2019) and have been shown to be closely linked to basin-scale changes in atmospheric circulation (Barnard et al., 2015; Wiggins et al., 2019b; Pfeffer et al., 2021). Climate variability, however, acts over multidecadal timescales and across wide regions, thus monitoring these temporal and spatial

* Corresponding author.
E-mail address: a.konstantiinou@plymouth.ac.uk (A. Konstantinou).

https://doi.org/10.1016/j.margeo.2023.107082
Received 1 December 2022; Received in revised form 3 April 2023; Accepted 3 June 2023
Available online 7 June 2023

scales of shoreline change poses significant challenges for both traditional, land-based survey methods (e.g., topographic beach surveying using GNSS or in-situ camera/video image analysis) and spatially broader remote sensing methods such as airborne LiDAR, and aerial photography (Mortlock and Goodwin, 2015; Burningham and French, 2017). As a result, continuous morphological records at adequate temporal (multi-decadal) scales are rare, particularly those accompanied by wave climate records, and are limited to a few sites around the world (e.g., Turner et al., 2016; Castelle et al., 2020).

Earth observation (EO) can now provide near global spatial coverage combined with moderate (10–30 m) spatial resolution and regular, short timescale (5–15 days) repeat measurements offering the opportunity for investigating shoreline evolution over decades at regional to global scales. Such large-scale analysis of shoreline behaviour can greatly enhance our understanding of the primary drivers of shoreline change and describe the relative importance of forcing mechanisms acting at different spatial scales, thus enabling improved projections of future shoreline dynamics (Castelle et al., 2021; Turner et al., 2021). Historically, the use of EO data for coastal applications has been limited by data access restrictions, computational requirements, and low spatial resolution of EO imagery. The opening of the Landsat archive in 2008 (Wulder et al., 2016) followed by the introduction of Sentinel-2A in 2015 and Sentinel-2B data in 2017, has allowed the coastal community access to these powerful datasets at no cost leading to the emergence of several data access platforms offering additional high-performance cloud computing capabilities such as Google Earth Engine (GEE) (Gorelick et al., 2017) and Data Access Cube (Dhu et al., 2017). The development of innovative analysis tools such as CASSIE (Almeida et al., 2021), SHOREX (Palomar-Vázquez et al., 2018), and CoastSat (Vos et al., 2019b) mean that 'analysis ready' EO data is now easily accessible at virtually no cost, presenting a unique and powerful tool for the historical study of shoreline change at local, region and even global scale.

Novel algorithms based on sub-pixel analysis have been used to resolve shoreline change at high spatial resolution and on timescales shorter than 6 months, overcoming the limitations of the relatively coarse spatial resolution (10–30 m) of current publicly available optical satellite data (Pardo-Pascual et al., 2012; Bishop-Taylor et al., 2019; Vos et al., 2019b). These advances have allowed mapping historical shoreline evolution over multiple decades on local (Garcia-Rubio et al., 2015; Almonacid-Caballer et al., 2016; Liu et al., 2017; Castelle et al., 2021), regional (Konlechner et al., 2020; Bishop-Taylor et al., 2021; Vos et al., 2021a), and even global scales (e.g., Hagenaars et al., 2018), demonstrating the potential of EO for long-term, large scale investigations. Luijendijk et al. (2018) and Mentaschi et al. (2018) proposed long-term (>30 yrs) global shoreline change trends providing an unprecedented insight into wide-scale shoreline dynamics. Although, the proposed trends seem to be reliable in certain areas, particularly where large, consistent changes occur, Castelle et al. (2021) highlighted that they seem to contradict field-based data and empirical evidence in slow evolving areas and sites with significant smaller-scale (e.g., intra-annual) variability and illustrated the impact of the SDS approach on the derived long-term trends.

Satellite-derived shoreline data is limited in certain areas due to lower satellite coverage and high cloud cover (Young et al., 2017; Sudmanns et al., 2020), amongst other factors, and is associated with large uncertainties relating to environmental factors including variability in the surrounding terrestrial zone, coastal substrate, sediment moisture, and grain size. The geolocation accuracy of satellite images also represents a singular source of error (O(10 m)) but one that is difficult to address as it varies both temporally and spatially around the globe (Storey et al., 2014; Languille et al., 2015; Choate et al., 2021). Tidal range and wave runup present additional challenges for satellite-based applications particularly at low-gradient sites (Garcia-Rubio et al., 2015; Hagenaars et al., 2018). Thus, both large scale applications and studies assessing the accuracy of satellite-derived shorelines have so far been largely restricted to specific settings, focusing on microtidal, sandy beaches at lower latitudes and/or synthetic shorelines (McAllister et al., 2022).

At their core, methods for the automatic optical remote sensing of the shoreline rely on the difference in the spectral signature between water and non-water surfaces to extract the land/water interface ('waterline') (e.g., Fisher et al., 2016). Although this boundary theoretically represents an idealised definition of the shoreline as expressed by Dolan et al. (1991), it is also highly dynamic and subject to continuous and diffuse change that reflects both morphological changes (e.g., due to cross-shore and alongshore sediment transport) and changes in the instantaneous water levels (e.g., due to tides, storm surge, wave setup and runup) (Boak and Turner, 2005). Consequently, shoreline position changes due to morphological variability need to be differentiated from those due to water level changes. The instantaneous nature of the waterline therefore presents a key challenge for image based SDS monitoring applications. Most studies, however, explicitly assume the influence of tidal elevation and wave action on the instantaneous local shoreline position is negligible (e.g., Kuleli et al., 2011; Pardo-Pascual et al., 2018; Cabezas-Rabadan et al., 2020). A common alternative approach for minimizing water level effects involves the aggregation of multiple images over specific time intervals for the creation of image composites (e.g., Luijendijk et al., 2018; Dai et al., 2019; Sayre et al., 2019). An obvious disadvantage of this approach is that the time interval over which images are aggregated also defines the temporal scale and type of phenomenon that can be studied (e.g., seasonal, annual, interannual). Additionally, this method inherently assumes equal sampling of all tidal stages and wave conditions within each composite image and the absence of spatial and/or temporal trends. Furthermore, the Nyquist rate for the spring-neap tidal cycle is 7.4 days which is smaller than even Landsat 5 (L5), Landsat 7 (L7), and Landsat 8 (L8) combined. While the revisit frequency of Sentinel-2 (S2) can be as low as 2–3 days, the influence of cloud cover can significantly increase sampling irregularity (Sudmanns et al., 2020; Vos et al., 2020). The combined effect is the introduction of tidal aliasing, with certain tidal stages being disproportionately sampled or potentially missed entirely.

These effects become increasingly important at low-gradient sites where small vertical changes in water level can result in hundreds of meters of horizontal shoreline translation and are enhanced by water-level fluctuations from high waves and/or large tidal range. The importance of considering these processes when extracting shorelines from satellite data (SDS) for a sandy, high-wave energy and meso-tidal beach was highlighted by Castelle et al. (2021) who found that wave run-up explained more than half of SDS error when only tidal elevation was considered. These authors also found that accounting for wave-induced water level fluctuations and tidal elevation, while excluding low tide images, reduced the RMSE to a third and the bias by half, stressing the importance of accounting for both processes. Consequently, large tidal fluctuations and energetic wave conditions present important challenges for image composite SDS applications, particularly at dissipative sites (Vos et al., 2019b; Castelle et al., 2021). As most SDS accuracy studies have been restricted by a narrow range of beach types, mostly at lower latitudes, the effect of morphological and hydrodynamic setting on SDS accuracy has not yet been fully addressed. Understanding the influence of beach type on the accuracy of the derived shorelines will increase our confidence in applying EO data to describe shoreline evolution, extract future shoreline change projections, and determine links between large scale climate patterns and coastal response.

In this paper, we address the influence of tidal elevation and wave-induced water-level fluctuations on the accuracy of satellite-derived waterlines (SDW), and corresponding satellite-derived shorelines (SDS), which result from the translation of the SDWs to a standard reference elevation. We use two sites representing end members of beach morphological type: Perranporth (macrotidal, dissipative, exposed, unidirectional wave incidence, cross-shore dominant transport) and Slapton Sands (macrotidal, reflective, semi-sheltered, bidirectional wave incidence, longshore dominant transport). We explore

the optimum water level parametrisation and assess the accuracy of the satellite-derived instantaneous waterlines (henceforth referred to as SDW) to minimize measurement uncertainty and therefore lead to an improved SDS determination. We investigate the accuracy of the satellite-derived shorelines translated to the optimum shoreline proxy (SDS) and assess the sensitivity of the SDS to the selected reference shoreline to determine the optimum shoreline proxy at each site. Finally, we propose an improved approach to extracting SDS and evaluate the quality of resulting long-term shoreline trends. This analysis is particularly relevant to applications in areas with little knowledge on beach morphology. These results have strong implications for local- to global-scale applications exploring seasonal and interannual shoreline variability and the extraction of long-term trends from optical satellite data.

2. Data and methods

2.1. Summary of approach to error analysis

We test the effect of tidal elevation and wave-induced water level fluctuations on the accuracy of satellite-derived shorelines (SDS), and

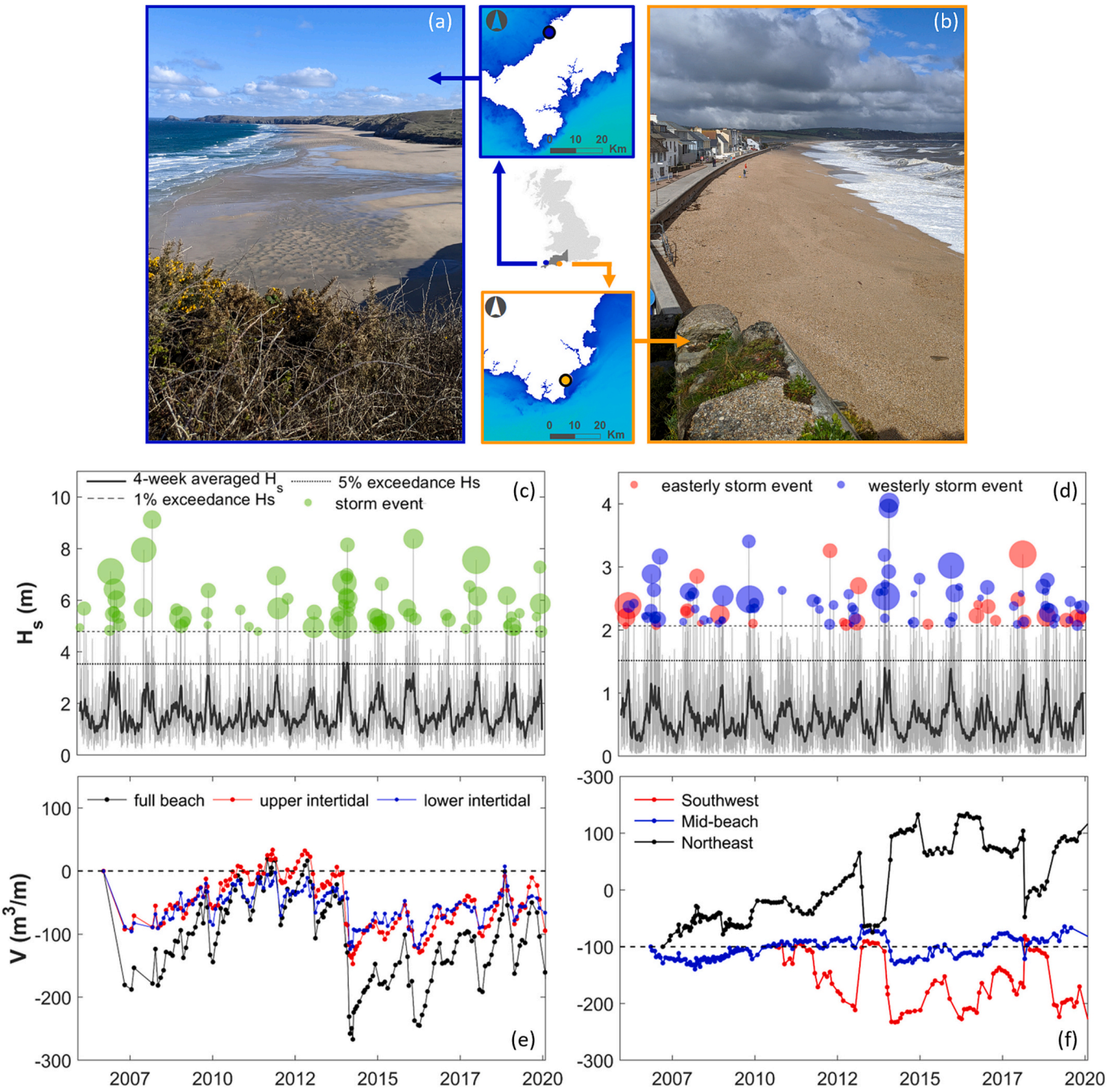

Fig. 1. Top: Site location and overview of Perranporth (a) and Slapton (b). Centre: Significant wave height for Perranporth (c) and Slapton (d). Wave data were derived from the Copernicus Marine Environmental Monitoring System dataset over the survey period (2006–2019) described in Section 2.5. Storms (coloured circles) are identified as events during which H_s exceeded the 1% exceedance wave height (4.8 m at Perranporth and 2.1 m at Slapton). Storm duration was defined as the period during which H_s remained above the 5% exceedance wave height (3.5 m and 1.5 m at Perranporth and Slapton). Bubble colour in (c) indicates southerly (blue) and easterly (red) mean storm direction. (e), (f): Beach volume time series derived from the quasi-monthly CPRG datasets described in Section 2.4.1 for Perranporth (e) and Slapton (f). (For interpretation of the references to colour in this figure legend, the reader is referred to the web version of this article.)

determine the most appropriate approach to extracting reliable SDS at each site using a two-step methodology:

(i) First, we establish the measurement accuracy of the extracted SDW for different water level parametrisations including the mean astronomic tidal level (η_0), instantaneous tidal elevation (η_t), tidal elevation plus wave setup ($\eta_{ts} = n_t + s$) and tidal elevation plus wave setup and runup ($\eta_{tsr} = \eta_t + s + r$).
(ii) Second, to enable temporal comparisons of the derived SDW, we project them to the most relevant shoreline contour at each site using a local beach slope estimate resulting in what is herein referred to as satellite-derived shorelines (SDS) and examine the sensitivity of the SDS to the selected contour.

2.2. Study sites

We explore the impact of morphological and hydrodynamic setting on the accuracy of SDS at two sites on the southwest coast of England with opposing characteristics. Perranporth beach (Fig. 1a, c, e) is located on the northern coast and is a high-energy (mean winter significant wave height $H_s = 2.02$ m; peak wave period $T_p = 12.1$ s; summer $H_S = 1.22$ m; $T_p = 9.2$ s), dissipative (($\tan\beta = 0.016$), macrotidal (spring tidal range of 6.3 m), sandy embayment ($D_{50} = 0.33$–0.40 mm). The dominant wave direction is near shore-normal from a westerly direction (285°) leading to a primarily cross-shore dominated sediment transport mechanism (Valiente et al., 2019). Beach volume from the monthly survey record at Perranporth shows a strong seasonal signal (O (100 m^3 m^{-1})) and significant underlying interannual (5–7 year) cycles (Fig. 1). The variability of the Mean Sea Level (MSL) shoreline position is almost 100 m (McCarroll et al., 2021).

In contrast, Slapton Sands (Fig. 1b, d, f) forms part of the larger Start Bay embayment on the south coast and is a meso- to macrotidal (mean spring tidal range of 4.3 m) gravel barrier beach ($\tan\beta = 0.13$; $D_{50} =$ 2.0–10.0 mm). Along most of its length, the barrier is backed by a freshwater lagoon. At its southernmost end, a sea wall protects a row of houses of Torcross village, while the northern end of the beach is backed by steep cliffs. This site is exposed to a moderate (winter mean $H_s = 0.9$ m; T_p of 9.1 s; summer mean $H_S = 0.48$ m; $T_p = 7.3$ s) bidirectional wave climate with the main direction from the southwest (150°–210°) and the secondary component from the east (80°–130°). As a result, it exhibits a typical rotational behaviour driven by the variability in the directional balance of easterly and southerly storms (Wiggins et al., 2019a). The beach volume time series derived from the monthly survey record at this site indicate significant underlying interannual cycles without a clear seasonal signal (Fig. 1f) that result in a long-term trend towards narrowing of the southern end (up to 1 m yr^{-1}) and widening of the northern end (up to 1 m yr^{-1}). The variability of the Mean Sea Level (MSL) shoreline position is an order of magnitude smaller compared to Perranporth (c.7.0 m).

Both sites have been monitored monthly since 2006 by the University of Plymouth's Coastal Processes Research Group (CPRG), and also bi-annually by the Plymouth Coastal Observatory (PCO) since 2007 as part of the UK Environmental Agency's coastal monitoring program (http://southwest.coastalmonitoring.org/).

2.3. Satellite data and waterline detection algorithm

We use CoastSat (Vos et al., 2019b), a python-based satellite shoreline detection toolkit available on GitHub (https://github.com/kvos/CoastSat), to extract the shorelines from Landsat-5 (L5), Landsat-7 (L7), Lansat-8 (L8), and Sentinel-2 (S2) images at the two sites. The tool allows the user to extract the land/water interface, that represents the instantaneous waterline, with an accuracy of 10–15 m (Vos et al., 2019a) and has been successfully used to extract the land/water interface in different coastal settings (Cuttler et al., 2020; Castelle et al., 2021; Heimhuber et al., 2021). A detailed description of the approach is provided in (Vos et al., 2019b) and a simplified schematic representation of the methodology is provided in Fig. 2. In this example, a characteristic low tide bar/rip system, resulting in a highly three-dimensional waterline is clearly visible. It should be noted that image registration, co-registration, and georectification were not performed.

A total of 1195 and 1011 images were available at Perranporth and Slapton, respectively. However, 399 (553) images at Slapton (Perranporth) were removed during the automatic filtering stage because of cloud cover exceeding 80% of the image surface area. A further 483 (314) images at Slapton (Perranporth) were not useful primarily due to: (1) light cloud cover and haze, not dense enough to be flagged as 'cloud', yet clearly sufficient to compromising the data; (2) cloud and cliff shadow on the shoreline; or (3) because of issues associated with dissipative sites that severely compromise water detection discussed extensively in Castelle et al. (2021). Of the remaining 293 images at Slapton, 147 (L5 = 23; L7 = 47; L8 = 38; S2 = 39) were within 30 days of a topographic beach survey, whereas of the 144 useable images at Perranporth, 93 (L5: 12; L7: 19; L8: 19; S2: 43) fell within 30 days of a survey (Fig. 4c,d).

2.4. Morphological data

Morphological data along specified transects shown in Fig. 3 was used to assess the accuracy of the extracted SDW and SDS and to determine the best shoreline proxy for each site.

2.4.1. Perranporth beach

CPRG conducts monthly intertidal and supratidal beach surveys covering the southern part of Perranporth beach (Perran Sands). The surveys are conducted with an All-Terrain Vehicle (ATV) equipped with a real-time kinematic global satellite navigation system (RTK-GNSS) and data is collected along a predefined grid (alongshore spacing: 250 m; cross-shore spacing: 25 m). The data is quality checked and reprocessed to a 5 m interpolated grid. Profile data was extracted from the gridded data along shore-normal transects (Fig. 3d) and combined with the quasi-biannual RTK-GNSS profile surveys conducted by the PCO on foot. A total of 155 CPRG and 31 PCO surveys between September 2006 and December 2019 were used (Fig. 4i).

2.4.2. Slapton sands

All data at Slapton Sands is collected using a pole-mounted RTK-GNSS. CPRG conducts monthly surveys, though not all profiles are included in every survey round. Once again, these data were combined with the quasi-biannual data collected by the PCO as part of the South West Coastal Monitoring Program. In all, data from 193 CPRG and 32 PCO surveys conducted between November 2006 and December 2019 were used (Fig. 4j).

2.5. Wave and water level data

Tidal elevation prediction time series for the two sites were extracted using the UK Hydrographic Office (UKHO) TotalTide™ v.5.0.4.9.4 (ATT, 2019) which provides harmonic tide predictions globally based on observed tidal records (Fig. 4e,f). Wave data was provided by the Copernicus Marine Environment Monitoring Service North West Shelf Wave Reanalysis hindcast (CMEMS, 2021), henceforth referred to as CMEMS. The CMEMS data is generated with a WaveWatch III (v.4.18) 1.5-km grid Atlantic Margin Model forced by the ECMWF-ERA5 wind model (Fig. 4a,b). The lateral boundary conditions are supplied by the UK Met Office global wave model hindcast and the model bathymetry is derived from EMODnet bathymetry (http://www.emodnet-bathymetry.eu). Wave parameters are available at a temporal resolution of 3 h on a regular 1.5-km gid (latitude) (Tonani and Saulter, 2020). Node locations at which the wave data for Perranporth and Slapton were extracted are indicated in Fig. 3a, and Fig. 3b, respectively.

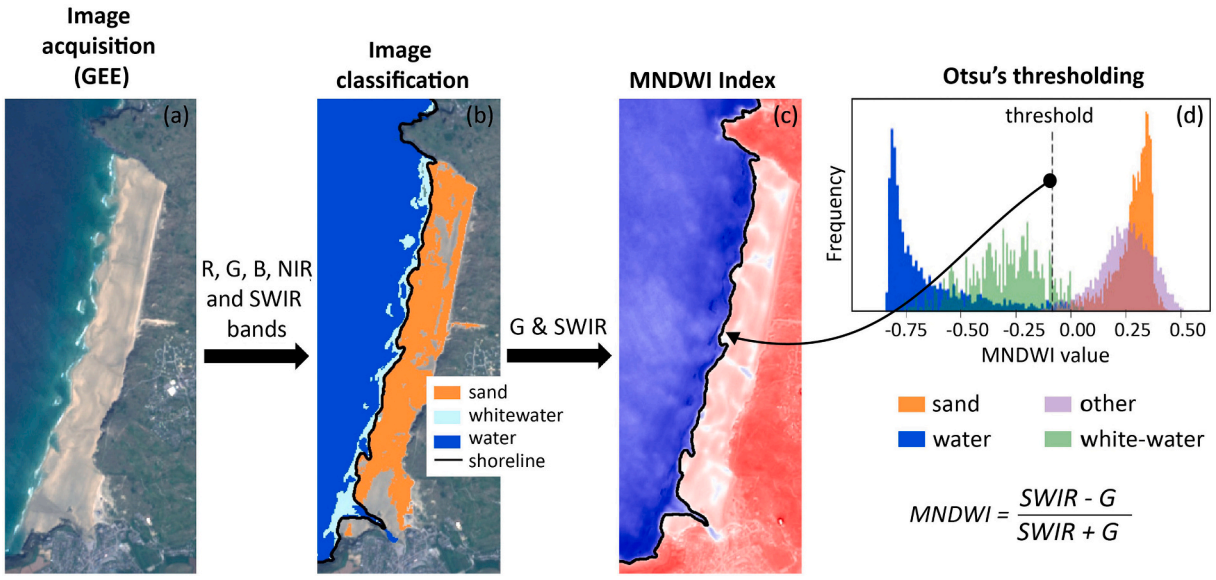

Fig. 2. Summary description of the CoastSat tool based on a S2 image captured at Perranporth on 27/05/2020. (a): the tool connects to GEE to download images based on used criteria; (b): information from five bands (R, G, B, NIR, and SWIR1) is used to classify the image into four classes; (c): The MNDWI raster is calculated; (d) Otsu's thresholding is applied on the histogram comprising only of sand and water pixels (Vos et al., 2019b).

2.6. Calculation of wave-induced water level fluctuations

The instantaneous water level at any given moment is defined by the sum of several components including tidal elevation, storm surge and wave induced water levels (e.g., wave set up, swash excursion). Here we consider three of these main components: (1) tidal elevation; (2) wave setup: the increase of water level at the shore due to wave breaking in the surf zone; and (3) wave runup: the maximum onshore elevation reached by waves relative to the shoreline position in the absence of waves. Wave runup is thus the result of the combination of wave setup and swash uprush. We test five different water level parametrizations to determine the optimal water level definition at image capture: (i) no consideration of water level fluctuations (η_0); (ii) including tidal elevation (η_t); (iii) including tidal elevation and wave setup (η_{ts}); and (iv) including tidal elevation, wave setup, and swash excursion (i.e., wave runup) (η_{tsr}). It should be noted that non-tidal residuals (atmospheric) were not considered as they were relatively small under most conditions during image capture (i.e., <0.1 m for more than 90% images) and have been shown not to improve SDS accuracy in similar environments (Castelle et al., 2021).

Wave setup/runup are a function of deep-water wave conditions but are also greatly affected by surfzone process (e.g., wave breaking, wave refraction) (Longuet-Higgins and Stewart, 1964) and tidal stage (Atkinson et al., 2017). They also behave differently under dissipative and reflective conditions (Ruggiero et al., 2001). As a result, a plethora of parametrizations have been proposed to empirically describe wave setup/runup from site-specific applications (e.g., Ruessink et al., 1998; Ruggiero et al., 2001; Senechal et al., 2011) to more generic estimates of wave setup/runup, typically in the form of maximum runup statistics. These formulations are generally based on deep-water wave parameters (e.g., wave period, wave height, and wave length) and beach face slope though do not necessarily include all of these (Atkinson et al., 2017). Perhaps the most widely used and extensively validated empirical models was developed by Stockdon et al. (2006). Their proposed model (Eq. (1)) has shown good performance in a range of different environments and wave conditions and was thus selected as most appropriate for the purposes of this study:

$$R_{2\%} = 1.1{*}0.35tan\beta H_o L_o + 1.1{*}0.5 H_o L_o \left[0.563(tan\beta)^2 + 0.004\right]^{0.5} \quad (1)$$

with L_o, H_o = the deep-water wavelength and height respectively; and $tan\beta$ = beach slope.

The first term in (Eq. (1)) represents setup ($S_{2\%}$) while the second term represents the swash excursion. The deep-water wave parameters required in the Stockdon equation were obtained by reverse-shoaling the extracted model data (Blenkinsopp et al., 2010) from the location of the model output nodes to a depth of 1000 m using linear wave theory. To ensure that the derived deep-water wave conditions accounted for the effects of nearshore wave transformation, wave direction and height at breaking were calculated prior to reverse shoaling (Stokes et al., 2021) (Fig. 4g,h). It should be noted that the wave runup formulations proposed by (Poate et al., 2016), specifically designed for gravel beaches was also tested. However, this formulation, which was specifically developed for extreme wave conditions, did not lead to improved SDW accuracy, and it was therefore decided to only use the Stockdon formulation for practical purposes. The value of tanβ used in (Eq. (1)) is a key unknown parameter. While beach face slope can be readily estimated from measured beach data (e.g., LiDAR, topographic), its determination on wider scales remains a significant challenge. Here, we use different approaches to determining tanβ in (Eq. (1)) depending on the application as described in Sections 2.7.1, 2.7.2, and 3.3.

2.7. Accuracy assessment

2.7.1. Measurement accuracy (SDW accuracy)

As a first step, we aim to determine the optimum water level parametrization for greatest SDW accuracy and assess the measurement accuracy of the SDW. As stated above, several different water level parametrisations were tested: a consistent water level equal to AMSL (η_0); the tidal elevation at image capture (η_t); tidal elevation and wave setup (η_{ts}); and tidal elevation, wave setup and runup (η_{tsr}). We further test the importance of wave shoaling and refraction prior to estimating η_{ts} and η_{tsr}. The nearest in time survey was used to establish the accuracy of the extracted SDW using the cross-shore distance between the cross-shore locations of the extracted SDW (W_{sat}) (Fig. 5a, red dot) and the estimated water level contour along each measured profile (Fig. 5a, black dot). Wave setup and runup in this case were calculated using an elevation-dependant, time-invariant slope calculated at each transect.

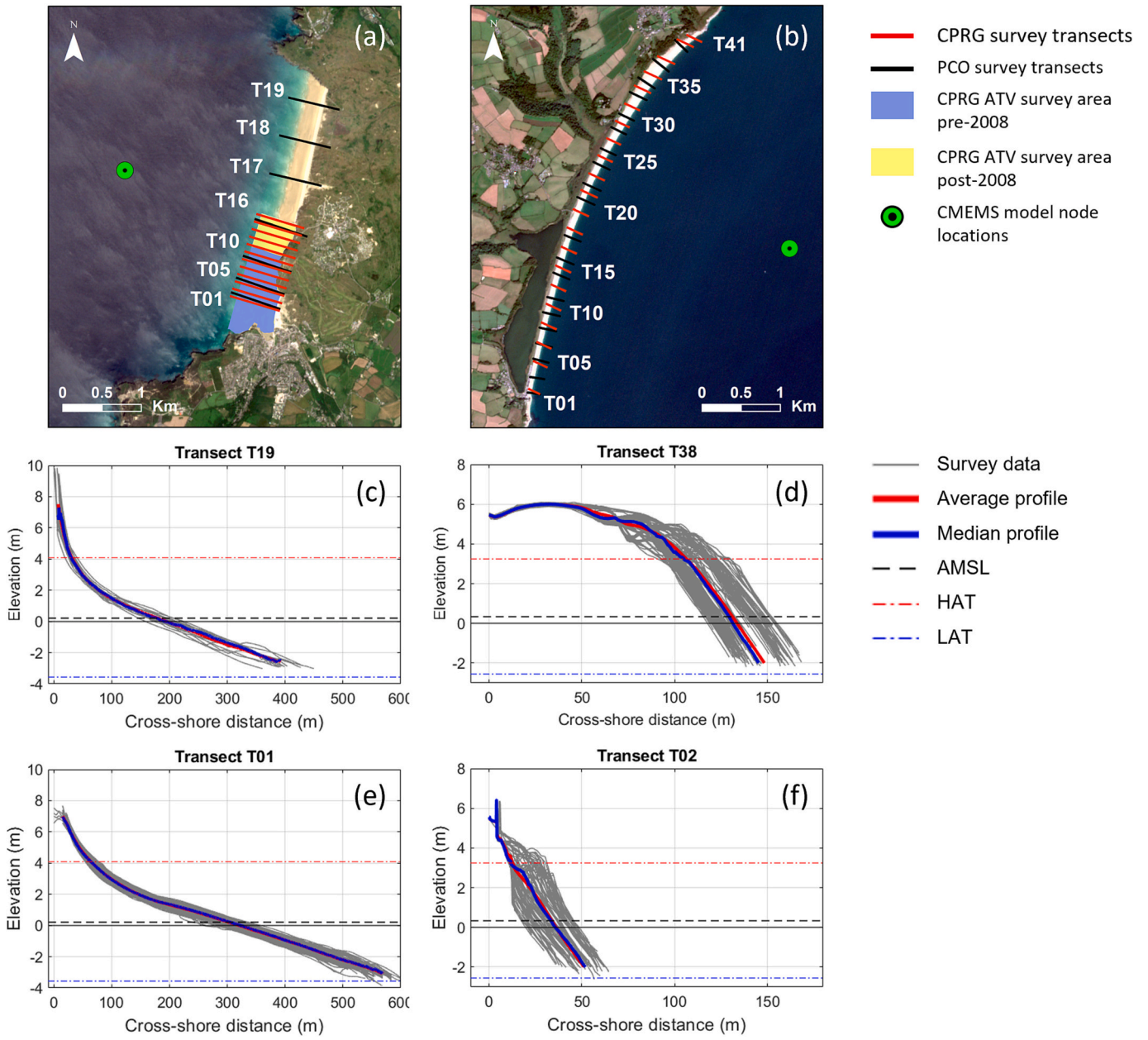

Fig. 3. Overview maps of the two study sites indicating the locations of the 1D survey profiles (red: CPRG transects; black: PCO transects), 2D survey areas, and locations of the wave model nodes for Perranporth (a) and Slapton Sands (b). Selected profile data at either end of the Perranporth beach (c), (e) and Slapton Sands (d), (f) including all survey profiles (grey), the mean (red) and median (blue) profiles. Astronomical mean sea level (AMSL), highest astronomical tide (HAT) elevations and lowest astronomical tide (LAT) elevations are also indicated. (For interpretation of the references to colour in this figure legend, the reader is referred to the web version of this article.)

2.7.2. Accuracy of projected shorelines (SDS accuracy)

Regardless of the precise interpretation, the instantaneous nature of the land/water interface precludes the comparison of temporally spaced shorelines. Therefore, SDWs are typically 'corrected' to a standard reference elevation, most often tidal datum-based (Yates et al., 2011; Lemos et al., 2018), to act as proxy to the real shoreline. This inevitably leads to the question as to which contour best reflects the morphology, dynamics and constraints of the environment of interest (Boak and Turner, 2005). While variability along the shoreline can be a useful proxy for describing subaerial volume change (Farris and List, 2007; Robinet et al., 2016) and overall change at the beach-face (Smith and Bryan, 2007), the relationship between changes in shoreline location and changes in beach volume vary, both spatially and temporally, depending on the selected shoreline indicator (i.e., reference elevation) (Stive et al., 2002). For a given beach, different shorelines seem to respond at different dominant timescales (Montano et al., 2021) driven by different processes (Castelle et al., 2014) and their correlation with beach volume can range from very weak ($R < 0.25$) to very strong ($R > 0.95$) (Robinet et al., 2016). Despite the significance of these observations, a scarcity of detailed assessments on the optimum shoreline proxy for any application and/or environment exists in the literature.

Therefore, prior to translating the SDW to a reference shoreline (SDS), we seek to determine the most appropriate reference shoreline elevation at each site by choosing the elevation contour that best correlates with changes in the overall intertidal beach volume. For this purpose, contours between 0.0 m AMSL and + 3.0 m AMSL were extracted from the survey datasets and their cross-shore position was correlated against beach volume from the monthly CPRG beach surveys.

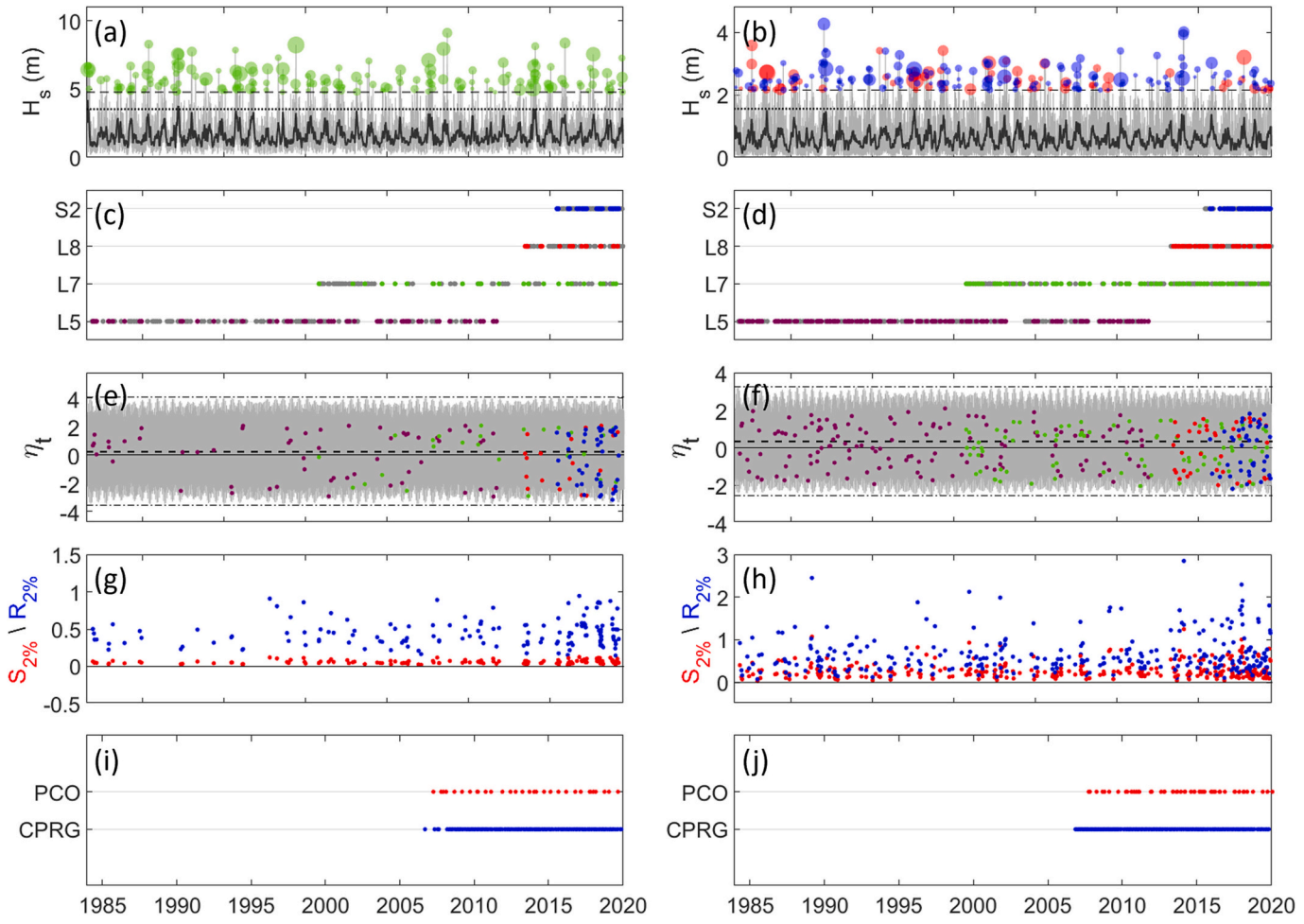

Fig. 4. Time series of: (a) (b) significant wave height (H_s); (c) (d) available satellite images after automatic filtering (grey) and final useable L5 (purple), L7 (green), L8 (red) and S2 (blue) images following further visual inspection (see text for details); (e) (f) tidal elevation (η_t) at the time of (useable) image capture, colour-coded according to satellite mission as in (c), (d); (g), (h): setup ($S_{2\%}$) and runup elevations ($R_{2\%}$) at satellite flyover; and, (i) (j) temporal coverage of CPRG and PCO surveys. Plots are presented for Perranporth (left) and Slapton (right). (For interpretation of the references to colour in this figure legend, the reader is referred to the web version of this article.)

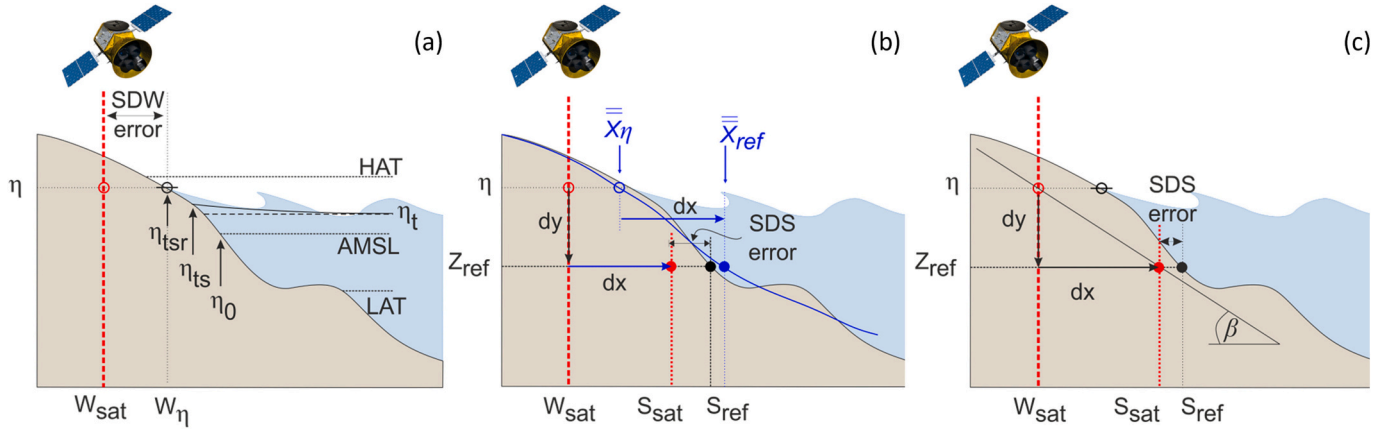

Fig. 5. (a). Graphic illustration of the different components of instantaneous water level (η). η_0: astronomical mean sea level (AMSL); HAT: highest astronomical tide; LAT: lowest astronomical tide; η_t: tidal elevation; η_{ts}: tidal elevation and wave setup; η_{tsr}: tidal elevation plus setup and swash. W_{sat} and X_η are the cross-shore locations of the SDW and η respectively. (b), (c): Translation of the instantaneous W_{sat} to the selected reference shoreline (S_{ref}): (b) using a temporally and alongshore-averaged beach profile (blue), where $\bar{X}_\eta$ ($\bar{S}_{ref}$) and the cross-shore location of the estimated water level (reference shoreline) on the average profile; and (c) using an estimated beach slope (tanβ). (For interpretation of the references to colour in this figure legend, the reader is referred to the web version of this article.)

This contour was then used as a reference or proxy shoreline to which the SDW from each satellite image was translated to obtain a consistent shoreline estimate from each image.

There are several ways of translating the SDW to the selected reference shoreline elevation (Z_{ref}), all of which require some knowledge of the profile morphology. Where adequate morphological data is available, it can be combined to derive a temporally averaged profile along each transect that can be used for determining the cross-shore distance between the estimated water level and the selected reference shoreline proxy (Fig. 5b). Such datasets are rare, and in the majority of cases there is little to no information on beach profile shape. At these sites, the SDW has to be translated using an estimated mean beach slope as shown in Fig. 5 (c). Although the latter option makes for a poor representation of beach morphology, it is a parameter that can be obtained using empirical formulas based on sediment size distribution (e.g., Flemming, 2011; Bujan et al., 2019), statistically based on existing extensive datasets (e.g., Bujan et al., 2019), or even from EO data (Vos et al., 2020), and can therefore be readily applicable to any site irrespective of the availability of measured data.

Where the average beach profile was used (Fig. 5b), S_{sat} was determined by translating W_{sat} by an amount equal to the horizontal distance (dx) as describe by (Eq. (2)):

$$dx = \bar{S}_{ref} - \bar{X}_{\eta} \tag{2}$$

where dx is the horizontal distance by which W_{sat} is translated to obtain S_{sat}. Note that the shift is negative onshore and positive offshore. $\bar{S}_{ref}$, $\bar{X}_{\eta}$ are the cross-shore locations of the intersections between the reference shoreline elevation and estimated water level contours respectively, and the average profile. Wave setup and runup in this case was calculated using a time-invariant, elevation-dependant slope at each profile.

When a fixed slope value was used to translate the SDW (Fig. 5c), the translation distance (dx) was determined as:

$$dx = \frac{Z_{ref} - \eta}{tan\beta} \tag{3}$$

where dx = horizontal distance by which W_{sat} is translated to obtain S_{sat}; Z_{ref} = elevation of the reference shoreline, η = the estimated water level at the time of image capture; and tanβ = the estimated beach slope, also used in (Eq. (1)) for the calculation of wave setup and runup.

In all cases, the satellite detected shoreline (SDS) error was calculated as the cross-shore distance between the S_{sat} (Fig. 5b, c: red dot) and S_{ref} (Fig. 5b, c: black dot) on the closest measured profile.

Although Vos et al. (2020) demonstrated that beach slopes can be derived by applying a frequency-based analysis to the SDW extracted with CoastSat (CoastSatSlope), this method was not tested on beaches with very low beach gradients ($tan\beta_{min} = 0.025$), requires a sufficient number of images (600 minimum) to perform successfully, and has been shown to perform poorly in tide-dominated (relative tidal range (RTR) $\geq$ 10) environments (Vos et al., 2021b). The SDS slope we derived at Perranporth using CoastSatSlope (tanβ = 0.09) confirmed these limitations suggesting that this approach is not universally applicable. We therefore obtained beach slopes using four different methods: (i) calculated between highest astronomical tide (HAT) and lowest astronomical tide (LAT) based on existing measured data; (ii) obtained using the second empirical relationship proposed by Bujan et al. (2019); (iii) beach slope values representing the 25th and 75th percentile D_{50} for sandy (0.125 mm $\leq$ D50 $\leq$ 0.5 mm) and gravel (0.125 mm $\leq$ D50 $\leq$ 0.5 mm) beaches as presented in Bujan et al. (2019) as representative of the upper and lower bound values for the two beach types. The obtained values for tanβ were used in both (Eqs. (1) and (3)).

As with the SDW, the derived SDS were compared to RTK-GNSS data collected within 30 days of image capture for each of the eight water level parametrizations described in Section 2.7.1. SDS error was calculated as the difference between the cross-shore location of the SDS (filled red dots in Fig. 5) and the intersection of the beach profile with the reference shoreline elevation S_{ref} (filled black dots in Fig. 5). Table 1 includes a list of symbols and abbreviations used throughout this study.

Table 1
List of symbols and abbreviations.

Symbol	Description
SDW	The instantaneous waterline extracted from satellite imagery.
SDS	SDW translated to a selected reference elevation. Acts a proxy for the real shoreline.
W_{sat}	Cross-shore location of the instantaneous satellite-derived waterline (SDW).
S_{sat}	Cross-shore location of the satellite-derived shoreline (SDS).
η	Instantaneous water level.
η_0	Instantaneous water level equal to astronomic mean sea level (AMSL).
η_t	Instantaneous water level equal to tidal elevation.
η_{ts}	Instantaneous water level equal to tidal elevation plus wave setup.
η_{tsr}	Instantaneous water level equal to tidal elevation plus wave setup and swash.
W_{η}	Cross-shore location of the estimated water level.
W_{η_0}, W_{η_t}, $W_{\eta_{ts}}$, $W_{\eta_{tsr}}$	Cross-shore location of the η_0, η_t, η_{ts}, η_{tsr} elevation contours respectively.
Z_{ref}	Selected reference elevation.
$S_{z_{ref}}$, $\bar{S}_{z_{ref}}$	Cross-shore location of the selected shoreline proxy on a measured profile and on a temporally averaged profile.

3. Results

3.1. Instantaneous waterline detection

The cross-shore locations of the satellite-derived waterlines (SDW) were systematically compared to the location of the various water-level parametrisations (Fig. 5) at fly-over time on the closest in time survey profile (W_{η}). Only image-survey pairs up to 30 days apart were used resulting in a total of 144 (93) image pairs at Slapton (Perranporth). All four main water level parametrisations described in Section 2.7.1 were used. Note that a positive bias would indicate the SDW (SDS) is further seaward, whereas a negative bias would indicate that the SDW is further landward from the cross-shore location of the estimated water level contour.

Fig. 6 shows the relationship between W_{sat} and W_{η} obtained along each transect for each useable satellite image over the survey period (2006–2019) at both sites and for each of the four water level parametrizations η, a summary of the SDW statistics is included in Table 2. The differences between the two sites are evident both in terms of the level of error and the effect of optimal water level corrections though the worst results across the board were obtained when no water level corrections were applied (see also Fig. 7). Significantly, the level of uncertainty at Perranporth when tidal elevation is not considered (η_0), is an order of magnitude higher compared to Slapton (Slapton RMSE = 18.1 m; Perranporth: RMSE = 138.2 m). Correcting for tidal stage (η_t) considerably improved results at both sites leading to a notable reduction in RMSE of 20% (3.7 m) at Slapton and 75% (117.8 m) at Perranporth (Fig. 6). At Perranporth, including wave runup (η_{tsr}) led to a further significant decrease of the RMSE by c. 35% (10.4 m) and the bias by over 75% (15.8 m). However, this parametrization had the opposite effect at Slapton where both the RMSE and bias increased (RMSE: c. +13% (1.9 m); bias: + c. 50% (3.9 m)), indicating that a different approach is required at the two sites.

Worth noting is the shift of the average location W_{sat} at Perranporth from 7.7 m seaward of η_0 to 20.3 m landward of η_t after tidal elevation was considered. This shift illustrates the effect of tidal aliasing due to the uneven sampling of tidal stages as a direct consequence of the revisiting frequency of the Landsat and Sentinel satellite series in relation to the tidal cycle (Sorensen, 2006). This effect is exacerbated by sampling irregularity due to cloud cover, and as tidal cycles, cloud and satellite

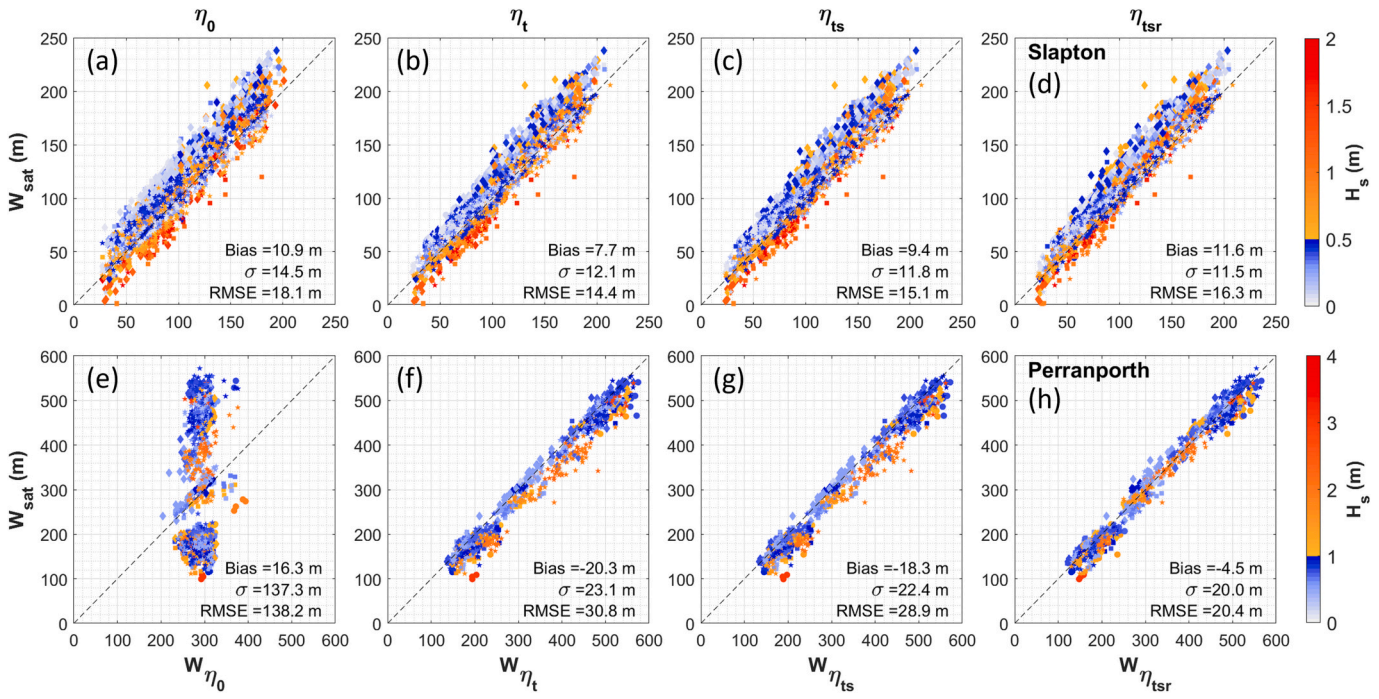

Fig. 6. Relationship between the cross-shore location of the elevation contour of each the four water level parametrizations tested, and the satellite-derived waterlines (SDW) extracted at every beach profile transect for each image/survey pair up to 30 days apart for Slapton (top) and Perranporth (bottom). The water level parametrizations (and corresponding cross-shore locations) shown are (a) and (e): η_0 ($W\,\eta_0$) = no correction; (b) and (f) η_t, ($W\eta_t$) = tidal elevation at image capture; (c) and (g) η_{ts}, ($W\eta_{ts}$) = tidal elevation and wave setup; (d) and (h) η_{tsr}, ($W\eta_{tsr}$) = tidal elevation and wave set up and runup. Colour is proportional to H_s. Units are in (m).

Table 2
Statistics of SDW against the location of the estimated water level along each transect (W_η) for each of the four water level parametrizations tested. Results are shown using all images (left) and only using images captured at water level (η_{tsr}) above astronomic mean sea level + 0.2 m (right).

	All images						η_{tsr} > AMSL+0.2					
	Slapton			Perranporth			Slapton			Perranporth		
	RMSE (STD) [m]	Bias [m]	n	RMSE (STD) [m]	Bias [m]	n	RMSE (STD) [m]	Bias [m]	n	RMSE (STD) [m]	Bias [m]	n
W_{η_0}	18.1	10.9	147	138.2 (137.3)	16.3	93	–	–	–	–	–	–
W_{η_t}	14.4	7.7	147	30.8 (23.1)	−20.3	93	15.4	8.7	69	28.5	−19.9	48
$W_{\eta_{ts}}$	15.4	9.2	147	28.9 (22.4)	−18.3	93	16.1	10.4	75	26.8	−18.3	48
$W_{\eta_{tsr}}$	16.3	11.6	147	20.4 (20.0)	−4.5	93	17.5	12.8	83	19.4	−6.8	50

coverage vary spatially, so will the impact of tidal aliasing on the accuracy of non-tidally corrected SDW.

Interestingly, filtering out images acquired at lower tidal elevations in order to avoid detection issues associated with dissipative sites as suggested by Castelle et al. (2021) and Vos et al. (2019b) did not notably improve performance at Perranporth (RMSE reduced by 1.0 m or 5%; |bias| increased by 2.3 m or 50%). A possible explanation that relates to the shape of the lower intertidal section of the beach profile is further discussed in Section 4.1. Importantly, both the filtered and unfiltered results indicated different optimal water level parametrizations at the two sites: best results at Slapton were obtained by only correcting for tidal elevation (η_t), while at Perranporth including wave setup and runup (η_{tsr}) significantly increased SDW accuracy. It should also be noted that results obtained at Perranporth without considering wave shoaling and refraction prior to reverse shoaling wave conditions for wave runup calculation, were associated with a higher RMSE by 2.2 m (i.e., c. +10%) and a three-fold seaward increase in mean bias (13.1 m), highlighting the importance of considering wave transformation processes.

A close inspection of the results revealed subtle, spatially variable differences in satellite performance at the two sites (Fig. 7). For the optimal water level parametrization at each site (Slapton: η_t; Perranporth: η_{tsr}), the S2 waterlines were consistently closer to the location of the estimated water level contour at both sites, as is reflected in Fig. 7b (Slapton) and Fig. 7e (Perranporth), and was also associated with the lowest RMSE (S2: 8.35 m and 18.1 m; L5: 15.8 m and 28.8 m; L7: 15.6 m and 23.0 m; and L8: 18.2 m and 19.1 m at Slapton and Perranporth respectively). Furthermore, results at Slapton also showed a clear spatial trend of decreasing accuracy towards the northern end of the beach (Fig. 7c). The observed satellite dependence of the ability to accurately detect the shoreline adds an additional level of uncertainty when considering decadal time series of satellite derived shoreline change.

These results revealed significant differences in measurement accuracy between the two morphologically contrasting sites in terms of the level of error and the optimal water level correction indicating that the optimal approach may be site-specific. The optimal strategy for the reflective site (Slapton) was to use η_t while at the dissipative site (Perranporth), considering wave-induced water level fluctuations by using η_{tsr} was critical. An important realization for the wider area of southwest England, which is probably relevant to other coastal areas with temperate or maritime climates, is the critically low image availability. To our knowledge, performance comparison between satellites at different locations has not been reported in the literature. Previous

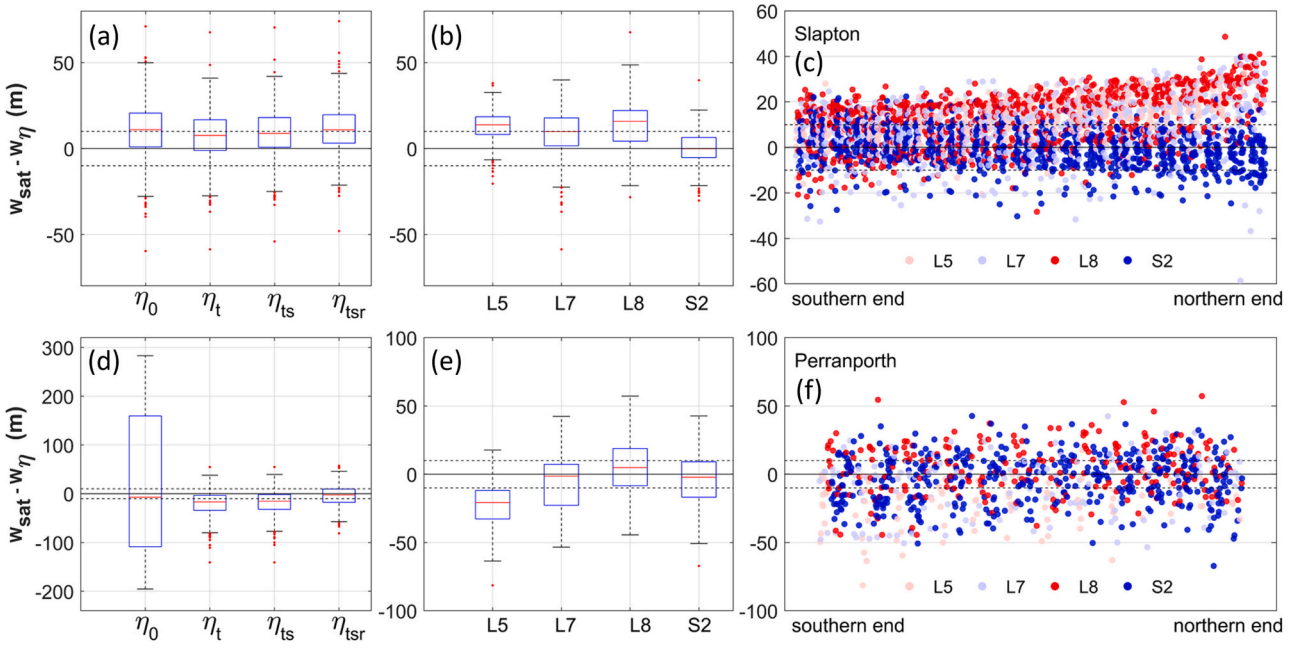

Fig. 7. Waterline detection error (SDW error) statistics for Slapton (top row) and Perranporth (bottom row). (a and d): SDW error for the four main water level parametrisations at each of the two sites; (b and e): Satellite performance shown for the optimum water level parametrization at (b) Slapton (η_t) and (e) Perranporth (η_{tsr}). The box plot boxes denote the interquartile range, maximum whisker extent is 1.5 times the interquartile range, while the red horizontal lines indicate the median values. Outliers, identified as points beyond maximum whisker length, are displayed as red dots. (c and f): SDW error plotted for the optimal water level parametrisation at each site indicating the satellite in different colours. Horizontal dashed lines indicate ± one pixel size (10 m). Units in (m). (For interpretation of the references to colour in this figure legend, the reader is referred to the web version of this article.)

studies on individual sites (e.g., Hagenaars et al., 2018; Vos et al., 2019b) report contrasting results which combined with the findings herein, imply that accuracy assessments may be location-specific and therefore, not widely applicable.

3.2. Assessment of best shoreline proxy

A first step to assessing SDS accuracy and deriving shoreline time series from the SDW, is determining which shoreline proxy is the most relevant one at either site. We define this here as the elevation contour that best correlates with beach volume based on the quasi-monthly CPRG data sets (Fig. 8). Overall, the shoreline position is a weaker indicator of overall beach volume at Slapton than it is at Perranporth (Slapton: $R_{max} = 0.61$; Perranporth: $R_{max} = 0.77$). This is perhaps not surprising as, in addition to its typical rotational response, Slapton beach features one and sometimes two berms, the location of which change considerably and at very short timescales, resulting in a noisy shoreline signal. When considering the two extremities of the beach separately, agreement increases by 10% (south: $R_{max} = 0.68$; north: $R_{max} = 0.66$). Intriguingly, while agreement at Slapton is stronger at 0.0 m above AMSL, at Perranporth, it is the 0.8 m (above AMSL) contour that best describes beach volume variability. When considering the corresponding elevation contour at Slapton (i.e., $S_{ref} = 0.8$ m), agreement is weaker ($R = 0.46$) though still significant.

3.3. Shoreline position (SDS) accuracy

Once the optimal water level parametrisations at each site have been defined (i.e., η_t for Slapton and η_{tsr} for Perranporth), the SDWs can be translated to a fixed shoreline elevation in order to quantify the horizontal displacement of the SDS through time. Only η_t and η_{tsr} are included in further analysis, ignoring therefore η_0 which led to the highest detection errors at both sites and η_{ts} which only slightly impacted results (Table 2). To determine the sensitivity of SDS to the selected reference shoreline, elevations between 0.0 m and 3.0 m above AMSL every 0.2 m were tested.

We first examine two methods of translating the W_{sat} to some reference shoreline: (i) using a time invariant, beach profile at each transect and (ii) using a (time invariant) mean beach slope calculated between HAT and LAT, a similar approach to that adopted by Vos et al. (2019a) and Castelle et al. (2021). We then translate the SDW to a range of reference shoreline elevations from 0.0 m to 3.0 m above AMSL. SDS error analysis using a temporally averaged profile, indicates that results at both sites are sensitive to the selected reference shoreline (Fig. 9). At Slapton, both RMSE and bias decreased with increasing elevation up to 2.4 m above AMSL where the lowest error was observed (RMSE = 13.7 m; bias = 5.3 m). This contour, however, showed a weak correlation with beach volume ($R < 0.3$). At Perranporth on the other hand, best results were obtained for elevation contours between 1.0 m and 1.6 m AMSL. At this site, the bias decreased from −5.8 m at 0.0 m elevation to −3.4 m at the 2.0 m elevation contour, while the RMSE was highest around the 0.4 m contour (RMSE = 24.5 m) and lowest between 1.0 and 1.6 m (RMSE = 22.1 m to 22.4 m). As elevation contours between 1.0 m and 1.4 m closely reflect subaerial volume changes ($R > 0.7$) at this site the 1.2 m elevation is considered to minimize error while still closely reflecting beach volume changes. The highest SDS accuracy at Slapton was once again achieved by only accounting for tidal elevation (RMSE = 13.7 m, bias = 5.3 m seaward for $S_{ref} = 2.4$ m), while including wave runup increased RMSE by c. 10% and the bias by c. 80%. At Perranporth in contrast, including wave runup (in addition to tidal elevation) reduced RMSE by c. 40% (from 31.1 m to 22.2 m) and the bias by c. 80% (from −20.2 m to −4.2 m landward), once again suggesting a different strategy is required for the two morphologically contrasting sites.

Table 3, summarises SDS error statistics for the optimal shoreline proxies at Slapton and Perranporth ($S_{0.0}$ and $S_{1.2}$ respectively) in terms of SDS accuracy. The evidently small compromises in accuracy suggest that using the AMSL contour across beach types may be considered optimal in terms of both SDS accuracy and representation of beach volume dynamics.

This method of translating the SDW (i.e., using a temporally average

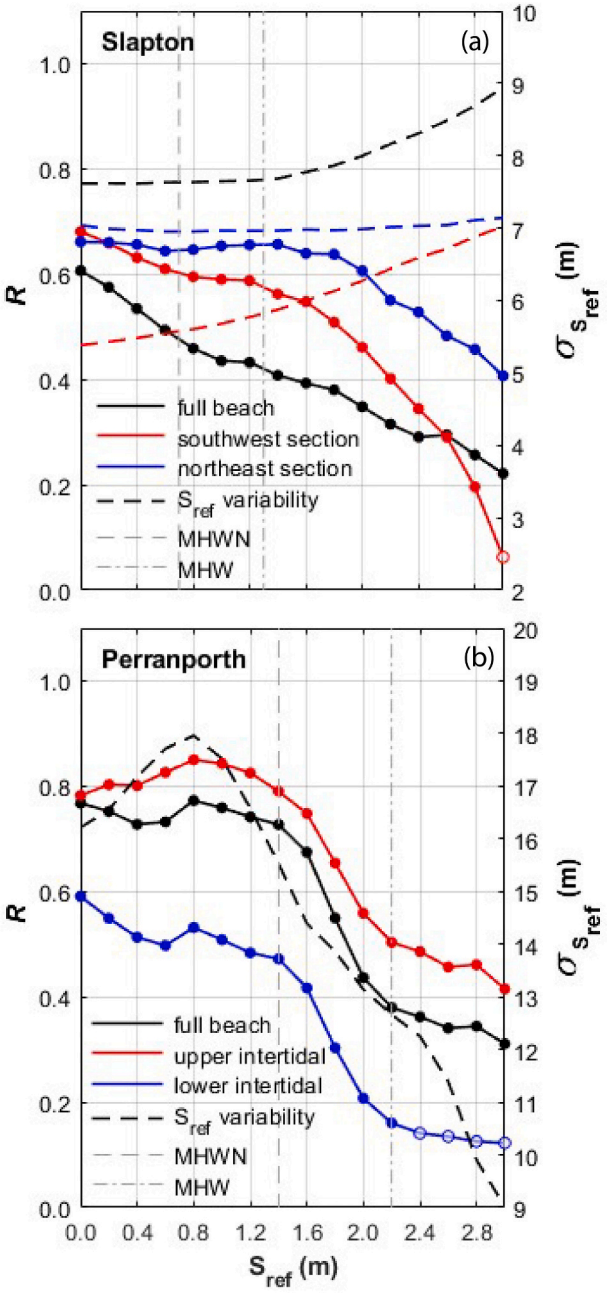

Fig. 8. Correlation R, between changes in beach volume and changes in the cross-shore location of elevation contours between 0.0 AMSL and 3.0 m above AMSL (S_{ref}) at (a) Slapton and (b) Perranporth (solid colour: significant to the 95% confidence level). To reflect the main modes of variability at the two beaches, at Slapton, correlations are shown for the southwestern and northeastern alongshore sections as well as for overall beach volume while for Perranporth, results are shown for the lower and upper intertidal section in addition to overall beach. The cross-shore variability of S_{ref} (σ_{Sref}) is at each elevation η is also shown (dashed lines).

beach profile) and therefore the above results, is only relevant to applications on sites where adequate morphological information is available and therefore has very specific applicability. More relevant to widescale (e.g., regional, global) applications is the use of an estimated beach slope for translating the SDW to a chosen SDS contour. Assessing SDS accuracy for these applications and its sensitivity to the value of the slope used is therefore of great value. Fig. 10 includes the results obtained for different values of beach slope for Slapton and Perranporth, calculated between LAT and HAT; using the empirical relationship proposed by Bujan et al. (2019); and using the 25th and 75th quartile beach slope values included in Bujan et al. (2019) for gravel and sandy beaches respectively. Note that in each case, wave runup was calculated using the same slope used for translating SDW.

Comparison of the accuracy (RMSE and mean bias) obtained using different waterline translation methods clearly indicate the importance of accurately defining beach slope. Results obtained at Slapton for the AMSL proxy shoreline were most consistent, with less than 1.0 m RMSE and 2.1 m bias attributed to the method used. However, at the 1.2 m proxy shoreline, the accuracy of the cross-shore SDS position from the various profile approximations increasingly diverged with increasing elevation, with the RMSE (mean bias) ranging from 13.4 m (11.6 m) and 17.0 m (11.6 m). The additional error induced in the Perranporth SDS results was more pronounced, with RMSE associated with the average measured slope being over 10 m higher than that obtained when using the mean profile and reaching 121.0 m when using the 75th quartile slope for sandy beaches (0.02). At both sites, the choice of waterline translation method had the least influence on SDS accuracy when AMSL was selected as the reference shoreline. At higher elevations however, the choice of translation method became increasingly important.

3.4. Shoreline change analysis

Fig. 11 shows the time series of alongshore-averaged shoreline positions relative to the long-term mean derived from the entire satellite dataset (1984–2020) for Slapton using η_t and Perranporth using η_{tsr} (Fig. 11d). SDS time-series for Slapton are shown for the entire beach (Fig. 11a) the southwest section (Fig. 11b), and the northeast section (Fig. 11c). The corresponding average measured shoreline is also shown ($S_{0.0\ m}$). Though the SDS signal is considerably noisier and does not consistently include an adequate number of images over the winter periods to capture seasonal variability, the results indicate strong intra-annual cycles of shoreline change. The shoreline trends calculated over the survey period at the southwest section based on the satellite data are similar to those derived from the survey data ($S_{\eta_{tsr}} = -1.27$ m yr^{-1}; $S_{1.2} = -1.06$ m yr^{-1}), while the corresponding long-term trend is slightly reduced (-0.66 m yr^{-1}), but of the same order. At the northern end of the beach, however, no significant trend in SDS was found despite the measured data showing a statistically significant trend of $+0.30$ m yr^{-1}. This may not be surprising as this section of the beach satellite shoreline detection was associated with greater uncertainty as discussed in Section 3.1. As a result, the SDS trends over the entire beach are larger than those derived from the survey data ($S_{\eta_{tsr}} = -0.98$ m yr^{-1}; $S_{0.0\ m} = -0.16$ m yr^{-1}) though still of the same order of magnitude (Fig. 11a).

The sparsity of data available at Perranporth is evident in Fig. 11d. The average number of useable images increased through time and ranged from less than 2 images per year before 1999 to over 14 images/year since the launch of S2 in 2015 while 8 of those years yielded less than 2 images each. Overall, between 1984 and 1999 when L7 became operational, only 29 useable images were available none of which were captured over boreal winter months (December to March) compared to a total of 62 images obtained since 2015, of which 5 were captured in winter months. At Slapton on the other hand, satellite useability was markedly higher, particularly over the pre-S2 era (84 images between 1984 and 1999; 119 between 2000 and 2014; 98 between 2015 and 2019). Though winter data at this site was not available for a third of the years up to 2013, at least three winter images were obtained every year since 2015. Consequently, limited data availability at both sites precludes the study of seasonal shoreline variability and may significantly influence long-term trends prior to 1999 at Perranporth, leading to questionable results.

4. Discussion

This study assessed the ability of existing satellite image analysis

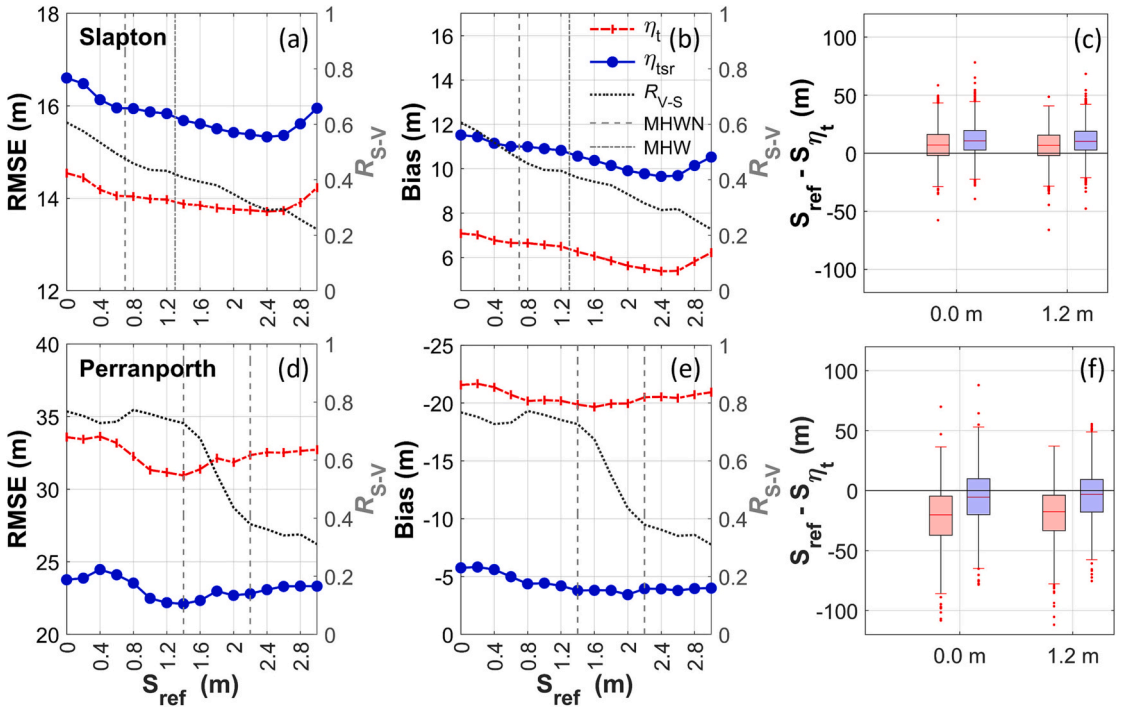

Fig. 9. Sensitivity analysis of SDS accuracy to reference shoreline elevations from 0.0 m to 3.0 above AMSL for Slapton (top) and Perranporth (bottom). RMSE (a and d) and mean bias (b and e) are plotted on the left-hand axis while the correlation of each elevation contour to beach volume is plotted on the right-hand axis (grey dashed line). Panels (c) and (f): Box plots of the difference between the satellite-derived shorelines (S_{sat}) and the most relevant elevation contour ($S_{0.0}$, $S_{1.2}$) and water level parametrisations (η_t: red); η_{tsr}: bleu) for each site. The boxes extend over the interquartile range and the red horizontal line marks the median value. The maximum whisker length is equal to 1.5 the interquartile range. Data points beyond maximum whisker extent are identified as outliers and shown as red dots. (For interpretation of the references to colour in this figure legend, the reader is referred to the web version of this article.)

Table 3
Statistics of SDS obtained by translating W_{sat} using an average beach profile for η_t and η_{tsr} and the cross-shore location of the 0.0 m AMSL ($S_{0.0}$) and 1.2 m AMSL ($S_{1.2}$) elevation contours. The optimum configuration at each site is indicated in bold.

	Slapton						Perranporth					
	η_t			η_{tsr}			η_t			η_{tsr}		
	RMSE (m)	STD (m)	bias (m)	RMSE (m)	STD (m)	bias (m)	RMSE (m)	STD (m)	bias (m)	RMSE (m)	STD (m)	bias (m)
$S_{0.0m}$	14.5	12.7	7.1	16.6	12.0	11.5	33.6	25.8	−21.6	23.8	23.1	−5.8
$S_{1.2\ m}$	**14.0**	**12.4**	**6.5**	15.8	11.6	10.8	31.1	23.7	−20.2	**22.2**	**21.8**	**−4.2**

technology to capture shoreline position change at relevant magnitudes and timescales for two different coastal environments in the United Kingdom. We address the influence of tidal elevation and wave-induced water-level fluctuations at two sites representing end members of beach morphological type in a region of low satellite useability (high cloud cover combined with low image availability). Results showed that defining an appropriate water level parametrisation significantly reduces uncertainty in SDS in macrotidal beach settings and revealed significant differences in SDS accuracy between the two morphologically contrasting sites in terms of the level of error and the optimal water level correction. Results further revealed different, and spatially variable performance between satellite sensors. We suggest that the optimal strategy for accurate SDS measurement may be site-specific and strongly controlled by beach state. Therefore, our findings have significant implications for both local- and large-scale applications that include a variety of different coastal environments as well as for the robustness and veracity of global-scale shoreline trends.

4.1. Beach state control

Our findings indicate that beach state is an important factor determining the relationship between shoreline position at different elevations and beach volume. At Perranporth, all elevation contours between AMSL and AMSL+1.4 m (roughly corresponding to MHWN), showed a high correlation with overall beach volume ($R > 0.7$). At Slapton on the other hand, shoreline position was generally a weaker indicator of beach volume change with the AMSL contour showing the highest correlation, reducing considerably with increasing elevation. Consequently, the elevation contours around MHW which are typically selected as shoreline proxies (Yates et al., 2011; Splinter et al., 2014; Kumar and Takewaka, 2019; D'Anna et al., 2021) may not be good indicators of beach volume change at reflective sites (Robinet et al., 2016; Montano et al., 2021). While different shoreline proxies best capture volume change at the two contrasting sites, the 0.0 m AMSL contour seemed to reflect beach volume changes readily at both beaches and may therefore provide a good compromise for larger-scale applications across beach types. However, the relationship between beach volume and shoreline position for different beach states remains largely unexplored.

Accounting for tidal elevation was crucial for the accurate detection of the instantaneous of waterline at both sites, leading to a notable reduction in both SDS and SDW RMSE of c. 20% at Slapton and c.75% at Perranporth. However, whilst including the wave runup component and thus characterising the water level fluctuation as fully as possible, was

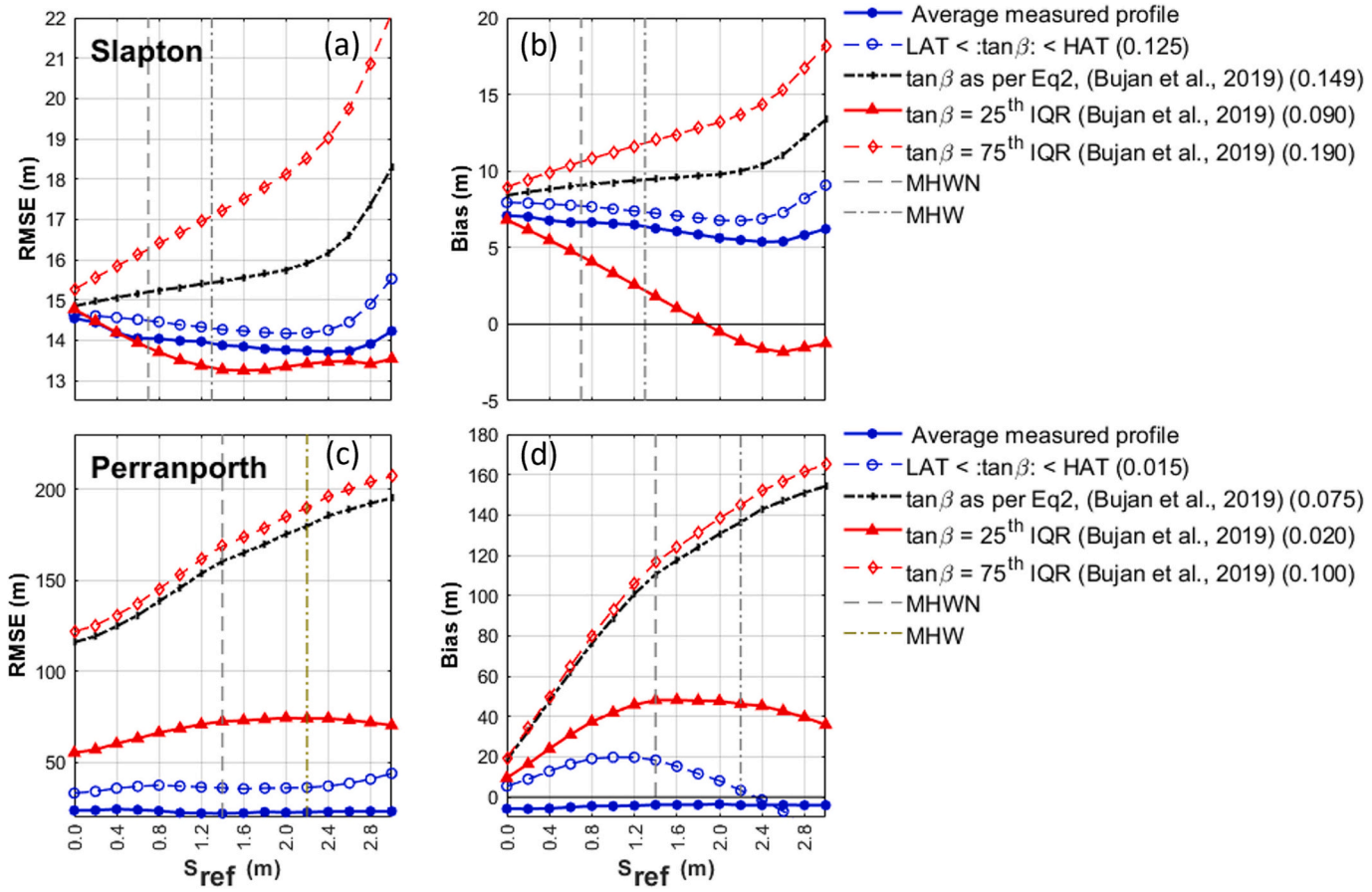

Fig. 10. Comparison of SDS (cross-shore) RMSE (left) and mean bias (right) for Slapton ($\eta = \eta_t$) and Perranporth ($\eta = \eta_{tsr}$) for a range of reference shorelines between AMSL and AMSL +3 m obtained using by using different methods for translating W_{sat}.

key to achieving significant accuracy improvement at the dissipative site (Perranporth), it was not advantageous at the reflective site (Slapton). We propose that that differences in the shape of the beach profile may provide an explanation for this apparently counterintuitive result. To illustrate, low gradient, high-energy sites like Perranporth have the potential for high wave runup extent. Hence, wave runup at this site explained 30% (85%) of SDS (SDW) variability and 75% (72%) of the mean offset at Perranporth, reinforcing the findings of Castelle et al. (2021). In addition, beaches of this type tend to remain wet and maintain patches of saturated sand confusing water detection algorithms that rely on spectral information to distinguish "land" from "water", explaining the resulting onshore shift of the detected waterline (mean bias 4.5 m) even when the full run-up is considered. In contrast, the combination of the steepness of the beach face at Slapton and sediment type eradicates the issue of saturation of the beach face but results in in a very narrow surfzone. Though alternative explanations have been proposed by various authors including factors relating to reflectance properties of the surrounding terrestrial zone (Pardo-Pascual et al., 2018), the presence of white water (Hagenaars et al., 2018) it is more likely that in the absence of white-water, which acts to facilitate the land/water delineation in the CoastSat algorithm, and the reflectance from the seafloor close to the waterline may lead to a seaward shift (mean bias 7.7 m) of the tidally corrected waterline as suggested by Pardo-Pascual et al. (2018). We further suggest that the extracted SDW at reflective beaches may closer reflect the downrush limit (i.e., close to the still water level) hence including wave-induced water level fluctuations does not improve results.

Furthermore, in contrast to the findings of, Castelle et al. (2021) and Vos et al. (2019b), images acquired at lower tidal elevations did not contribute significantly to SDW uncertainty at the dissipative site (RMSE reduced by 1.0 m or 5%; |bias| increased by 2.3 m or 50%). A possible explanation relates to the shape of the lower intertidal section of the beach profile. Morphodynamically, Truc Vert is classed as an intermediate, double bared system (Castelle et al., 2007). The inner (intertidal) rip/bar system is classed as modally as a transverse bar/rip and tends to attach to the beach as a low-tide terrace system under low energy conditions especially during summer periods (Castelle et al., 2007). The average intertidal beach slope is 0.05 and ranges between c.0.02 along the lower part of the profile to c. 0.11 in the upper part of the beach (Castelle et al., 2021). This progressive flattening of the beach in the lower intertidal area often results in the exposure of the inner bar/rip system, in turn resulting in highly non-uniform and irregular instantaneous SDWs. For beaches in this state, low-tide SDWs may introduce higher uncertainty simply as a result of the morphology of the intertidal beach profile. In contrast, the shape of the upper lower intertidal beach profiles at both Perranporth and Slapton is fairy uniform (Fig. 3c,e and Fig. 3d,f respectively), so the contribution of low-tide images is comparable to that of all other tidal stages. Consequently, at sites where the beach profile, whether concave or convex, has a fairly uniform lower intertidal profile, it is possible to use all useful images, irrespective of tidal stage at image capture.

Beach profile shape, and thus beach state, play an important role in the definition and accuracy of the SDW, and in the overall SDS accuracy. How different shoreline proxies capture volume change is also a function of beach state and SDS accuracy was found to be sensitive to the selection of reference shoreline elevation and varied with both beach type and shoreline translation method. The highest SDS accuracy was achieved by using an average profile for translating W_{sat} to a reference shoreline with the optimal approach varying between sites, indicating that a different strategy is required for the two morphologically

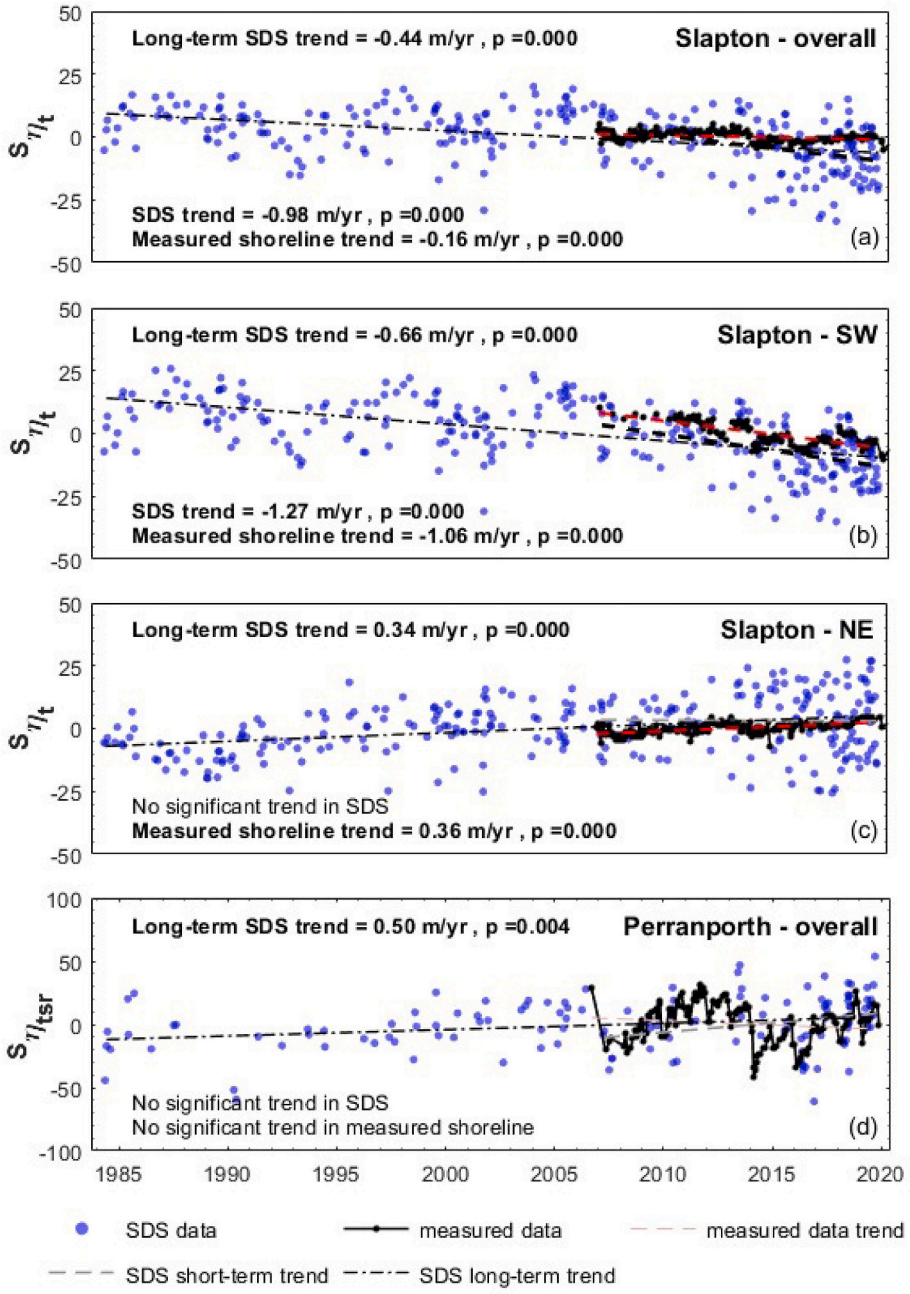

Fig. 11. Time series of satellite-derived shoreline position relative to the long-term mean obtained for Slapton (η_t) and Perranporth (η_{tsr}) for the 0.0 m AMSL proxy shoreline. (a-c): shoreline location at Slapton averaged across (a): the entire beach; (b): Slapton southwest section; (c) the northeast section. (d): Alongshore average shoreline location at Perranporth. SDS are shown in blue, while the location of $S_{1.2}$ based on the measured survey data is shown in black. The derived trends over the survey period are shown at the bottom of each panel while the long-term (1984–2019) trends are shown at the top. The significance of the time-series trends is based on a two-tailed *t*-test at 99% significance level. (For interpretation of the references to colour in this figure legend, the reader is referred to the web version of this article.)

contrasting sites (Table 3). Although a direct comparison cannot be performed, results obtained using the same shoreline detection tool at sites with different characteristics (tidal range, beach slope, sediment size) included in Table 4 provide support for this finding. At sites with large tidal ranges (Truc Vert, Slapton, Perranporth) considering the tidal elevation at image capture is key. Similarly, at high energy, dissipative (Perranporth and Truc Vert), including wave runup essential.

For large-scale applications or when extracting shorelines at sites with little or no information, linear translation using (Eq. (3)) with some measure of beach slope is the only available option for translating W_{sat} to a reference shoreline. The level of error associated with this method however was strikingly higher and greatly influenced the selected shoreline proxy at both sites, potentially increasing uncertainty 10-fold. The associated uncertainties in this case are a function of both detection errors and the deviation of beach-face geometry from the theoretical line defined by (Eq. (3)). At both sites the lowest error was associated with the AMSL proxy shoreline. This was perhaps expected as using higher (or lower) elevations would exaggerate errors relating to beach-face geometry and the location of berms and/or steps for example. It is therefore suggested that when linear translation is applied, the AMSL shoreline proxy should be used. It should be noted that the lower error associated with the 25th percentile slope value based on D_{50} (0.09) at Slapton (Fig. 10) is most probably a result of the combination of the mean seaward bias observed at this site with a lower slope than the actual (Slapton: measured $\tan\beta = 0.125$). These findings have significant implications for both local- and large-scale applications as they indicate that errors in order of 10s to 100 s of meters may be incurred depending on the approach used for a given application. Consequently, the question as to which approach is suitable for a given application is raised. Table 5 below includes a summary of suggested SDS strategies for different applications.

Table 4
Summary of SDS strategy and accuracy in SDS using CoastSat reported at sites with different characteristics.

		Reflective		Dissipative	
Site (publication)		Moruya (Vos et al., 2019b)	Slapton Sands (this work)	Truc Vert (Castelle et al., 2021)	Perranporth (this work)
Site characteristics	Tidal range	1.3 m	4.4 m	3.7 m	6.3 m
	tanβ	0.1	0.13	0.05	0.015
	D50	0.35 mm	2–10 mm	0.35 mm	0.34 mm
SDS strategy	Water level correction	None	tidal elevation	tide + full runup	tide + full runup
	Image filtering	Automatic	automatic & manual	automatic & manual	automatic & manual
	Water level filtering	None	none	AMSL+0.2 m	None
	Proxy shoreline	No translation	1.2 m AMSL (~MHW)	1.5 m AMSL (~MHW)	1.2 m AMSL (~MHWN)
	W_{sat} translation method	n/a	average profile	alongshore averaged, elevation-dependant slope	average profile
Accuracy	RMSE	11.6 m	14.0 m	10.3 m	22.2 m
	bias	11.6 m	6.5 m	7.1 m	- 4.2 m
Accuracy with no water level correction	RMSE	11.6 m	18.1 m	31.4 m	138.2 m
	bias	11.6 m	10.2 m	22.5 m	16.2 m
		Microtidal		*meso- to macrotidal*	

Table 5
Summary of suggested optimal SDS strategy for different applications in meso-macrotidal regions and potentially low satellite useability: local applications on individual sites with long-term morphological data; mixed applications including a range of sites where long-term data is available; large-scale applications where SDS are extracted for a variety of different beach type with little to no information on beach morphology.

Water level definition	Local applications		Mixed applications	Large scale
	Reflective	Dissipative		
	η_t	η_{tsr}	η_{tsr}	η_{tsr}
W_{sat} translation	average profile	average profile	average profile	linear translation
Proxy shoreline	MHW	MHWN	MHWN-MHW	AMSL
RMSE	1.5 pixel	2 pixels <	2 pixels <	12 pixels
Bias	< 1 pixel (seaward)	< 0.5 pixels (landward)	≈ 1 pixel	7 pixels

4.2. Long-term shoreline analysis

In many high latitude regions, and areas with low satellite useability, the critically low image availability restricts temporally the type of phenomenon that can be detected (e.g., seasonal variability, storm impact) and may compromise computed long-term trends when appropriate data is not available (absence/aliasing). Nevertheless, when an optimal strategy was applied, SDS data effectively reproduce observed trends (or lack of) over the survey period (2006–2019) at both study sites. However, sparse and intermittent data prior to the launch of L7 in 1999, reduced reliability of long-term trends derived from the dissipative site. The observed differences in satellite performance discussed in Sections 3.1 and 4.1 add an additional level of uncertainty when considering decadal time series of satellite derived shoreline change.

Though we recognise the importance of these pioneering global-scale applications in paving the way for utilizing EO data for coastal studies, it is likely these assessments have incurred significant shoreline detection errors, equal to or larger than the trends or fluctuations reported. Although a direct comparison is not possible, a brief inspection of the mean linear rates of change (LRC) published by Luijendijk et al. (2018) (available at: http://shorelinemonitor.deltares.nl) reveal major differences. For example, at two adjacent transects on the southern end of Slapton, the reported LRC was -4.8 ± 2.0 m yr^{-1} and -11.1 $\pm$ 4.5 m yr^{-1} whereas our results show long-term trends ranging between -3.4 and -3.9 m yr^{-1} over the same area of the beach. Although seemingly results for the first transect are comparable, shoreline locations derived by the former authors' range from 0 m to -600 m and -1000 m to -100 m respectively for the two transects that cover a section of beach with a maximum width of 70 m. It is therefore clear that the resulting SDS have been compromised, possibly due to cloud cover, atmospheric interference or local factors including the presence of a coastal lagoon despite the use of image compositing, a technique applied to overcome such effects. Furthermore, the dataset also features intermittent data (e.g., only one data point between 1990 and 1997) rendering extracted trends along these transects questionable. These observations highlight the importance of SDS strategy (i.e., water level definition, SDS translation method, and image filtering) for the derivation of reliable trends that enable improved future projections (Castelle et al., 2018; Turner et al., 2021).

4.3. Limitations

It is necessary to recognise that the manual image filtering stage is inadvertently open to interpretation error as the distinction between 'useable' and 'not-useable' images involves subjective decision making on behalf of the researcher. However, this subjectivity is compensated for by increased confidence in the analysis. An additional, evident limitation relates to the need for auxiliary water level data. In the absence of long-term measured data, long-term applications rely on model data for both tidal elevation and wave parameter data, the quality of which varies around the globe (Maraldi et al., 2013; Stammer et al., 2014; Zaron and Elipot, 2021). Furthermore, and in contrast to most coastal applications where the statistical wave and tide parameters are of interest, SDS applications require instantaneous values corresponding to the time of image capture. As such, discrepancies on timing add to the potential for differences in estimated water levels and may significantly impact SDS accuracy particularly at dissipative sites and/or sites with large tidal ranges. The geolocation accuracy of satellite images also represents a singular source of error (O(10 m)) and one that varies spatially around the globe (e.g., Choate et al., 2021). Therefore, co-registration of images may be required in certain locations prior to shoreline extractions. Because the geolocation accuracy of satellite images is also temporally variable, this process has very high computational requirements, especially for large-scale applications (Palomar-Vázquez et al., 2018; Sánchez-García et al., 2020).

5. Conclusions

In this study we explore the influence of to investigate the influence of tidal elevation and wave action on SDS accuracy at two sites in the southwest of England representing end members of beach morphological type. Our findings reveal that:

- The optimal approach for accurate waterline detection from satellite imagery is crucial for accurate shoreline measurement and largely controlled by beach state;
- SDS accuracy is sensitive to the selection of reference shoreline elevation and that the optimal approach depends on the shoreline translation method used and is therefore different depending on the type of application;
- Low satellite image usability in some locations can have serious implications restricting the type of phenomenon that can be detected and potentially introducing tidal aliasing;
- Our findings imply that a one-size-fits-all approach adopted in previous large or global scale assessments may lead to incorrect conclusions about shoreline dynamics.

We suggest that translating satellite detected waterline to 0.0 m AMSL contour can provide a good balance between accuracy and representation of volumetric change and is recommended as comparable elevation for other studies of coastal dynamics. We therefore propose variable SDS strategies to increase confidence in SDS extraction in meso-macrotidal environments with potentially low satellite useability depending on the spatial scale of the intended application.

Declaration of Competing Interest

The authors declare that they have no competing financial interests or personal relationships that may have influenced the work presented in this paper.

Data availability

Satellite-derived data were obtained using CoastSat v1.2 and are available at https://github.com/kvos/CoastSat. The data obtained using CoastSat and in-situ data used in this study can be found at ZENODO open access repository (doi:https://doi.org/10.5281/zenodo.7383895). The wave hindcast data used are included in the Copernicus Marine Environment Monitoring Service (CMEMS) NWSHELF_REANALYSIS_WAV_004_015 product can be found at https://marine.copernicus.eu/. Tidal elevation data are provided by the UK Hydrographic Office (UKHO) TotalTideTM v.5.0.4.9.4 and are commercially available via https://www.admiralty.co.uk/.

Acknowledgements

This work was supported by UK Natural Environment Research Council grant (NE/M004996/1 Masselink; BLUE-coast project). BC is funded by Agence Nationale de la Recherche (ANR) grant number ANR-21-CE01-0015. Our thanks go to all the CPRG members and University of Plymouth students who have been, and still are, contributing their efforts to the CPRG beach survey program. We would also like to thank Kilian Vos and the Water Research Laboratory for developing and making freely available the CoastSat toolkit and for their support.

References

Allen, J.R.L., 2000. Morphodynamics of Holocene salt marshes: a review sketch from the Atlantic and Southern North Sea coasts of Europe. Quat. Sci. Rev. 19 (12), 1155–1231. https://doi.org/10.1016/s0277-3791(99)00034-7.

Almeida, L.P., de Oliveira, I.E., Lyra, R., Dazzi, R.L.S., Martins, V.G., da Fontoura Klein, A.H., 2021. Coastal Analyst System from Space Imagery Engine (CASSIE): shoreline management module. Environ. Model. Softw. 140, 105033. https://doi.org/10.1016/j.envsoft.2021.105033.

Almonacid-Caballer, J., Sánchez-García, E., Pardo-Pascual, J.E., Balaguer-Beser, A.A., Palomar-Vázquez, J., 2016. Evaluation of annual mean shoreline position deduced from Landsat imagery as a mid-term coastal evolution indicator. Mar. Geol. 372, 79–88. https://doi.org/10.1016/j.margeo.2015.12.015.

Anfuso, G., Loureiro, C., Taaouati, M., Smyth, T., Jackson, D., 2020. Spatial variability of beach impact from post-tropical cyclone Katia (2011) on Northern Ireland's North Coast. Water 12 (5), 1380. https://doi.org/10.3390/w12051380.

Atkinson, A.L., Power, H.E., Moura, T., Hammond, T., Callaghan, D.P., Baldock, T.E., 2017. Assessment of runup predictions by empirical models on non-truncated beaches on the south-east Australian coast. Coast. Eng. 119, 15–31. https://doi.org/10.1016/j.coastaleng.2016.10.001.

ATT, 2019. NP201B Admiralty Tide Tables: United Kingdom and Ireland, Vol. 1B. United Kingdom Hydrographic Office, UK.

Barnard, P.L., Short, A.D., Harley, M.D., Splinter, K.D., Vitousek, S., Turner, I.L., Allan, J., Banno, M., Bryan, K.R., Doria, A., Hansen, J.E., Kato, S., Kuriyama, Y., Randall-Goodwin, E., Ruggiero, P., Walker, I.J., Heathfield, D.K., 2015. Coastal vulnerability across the Pacific dominated by El Nino/Southern Oscillation. Nat. Geosci. 8 (10), 801. https://doi.org/10.1038/ngeo2539.

Bishop-Taylor, R., Sagar, S., Lymburner, L., Alam, I., Sixsmith, J., 2019. Sub-Pixel waterline extraction: characterising accuracy and sensitivity to indices and spectra. Remote Sens. 11 (24), 23. https://doi.org/10.3390/rs11242984.

Bishop-Taylor, R., Nanson, R., Sagar, S., Lymburner, L., 2021. Mapping Australia's dynamic coastline at mean sea level using three decades of Landsat imagery. Remote Sens. Environ. 267, 19. https://doi.org/10.1016/j.rse.2021.112734.

Blenkinsopp, C.E., Mole, M.A., Turner, I.L., Peirson, W.L., 2010. Measurements of the time-varying free-surface profile across the swash zone obtained using an industrial LIDAR. Coast. Eng. 57 (11), 1059–1065. https://doi.org/10.1016/j.coastaleng.2010.07.001.

Boak, E.H., Turner, I.L., 2005. Shoreline definition and detection: a review. J. Coast. Res. 21 (4), 688–703. https://doi.org/10.2112/03-0071.1.

Brooks, S.M., Spencer, T., 2014. Importance of decadal scale variability in shoreline response: examples from soft rock cliffs, East Anglian coast, UK. J. Coast. Conserv. 18 (5), 581–593. https://doi.org/10.1007/s11852-013-0279-7.

Bujan, N., Cox, R., Masselink, G., 2019. From fine sand to boulders: Examining the relationship between beach-face slope and sediment size. Mar. Geol. 417, 106012. https://doi.org/10.1016/j.margeo.2019.106012.

Burningham, H., French, J., 2017. Understanding coastal change using shoreline trend analysis supported by cluster-based segmentation. Geomorphology 282, 131–149. https://doi.org/10.1016/j.geomorph.2016.12.029.

Cabezas-Rabadan, C., Pardo-Pascual, J.E., Palomar-Vazquez, J., Ferreira, O., Costas, S., 2020. Satellite derived shorelines at an exposed Meso-tidal beach. J. Coast. Res. 1027–1031. https://doi.org/10.2112/si95-200.1.

Castelle, B., Bonneton, P., Dupuis, H., Sénéchal, N., 2007. Double bar beach dynamics on the high-energy meso-macrotidal French Aquitanian Coast: a review. Mar. Geol. 245 (1), 141–159. https://doi.org/10.1016/j.margeo.2007.06.001.

Castelle, B., Marieu, V., Bujan, S., Ferreira, S., Parisot, J.P., Capo, S., Senechal, N., Chouzenoux, T., 2014. Equilibrium shoreline modelling of a high-energy meso-macrotidal multiple-barred beach. Mar. Geol. 347, 85–94. https://doi.org/10.1016/j.margeo.2013.11.003.

Castelle, B., Dodet, G., Masselink, G., Scott, T., 2018. Increased winter-mean wave height, variability, and periodicity in the Northeast Atlantic over 1949–2017. Geophys. Res. Lett. 45 (8), 3586–3596. https://doi.org/10.1002/2017GL076884.

Castelle, B., Bujan, S., Marieu, V., Ferreira, S., 2020. 16 years of topographic surveys of rip-channelled high-energy meso-macrotidal sandy beach. Sci. Data 7 (1), 9. https://doi.org/10.1038/s41597-020-00750-5.

Castelle, B., Masselink, G., Scott, T., Stokes, C., Konstantinou, A., Marieu, V., Bujan, S., 2021. Satellite-derived shoreline detection at a high-energy meso-macrotidal beach. Geomorphology (Amsterdam, Netherlands) 383, 107707. https://doi.org/10.1016/j.geomorph.2021.107707.

Choate, M.J., Rengarajan, R., Storey, J.C., Lubke, M., 2021. Geometric calibration updates to landsat 7 ETM+ instrument for landsat collection 2 products. Remote Sens. 13 (9), 1638. https://doi.org/10.3390/rs13091638.

Clemmensen, L.B., Nielsen, L., Bendixen, M., Murray, A., 2012. Morphology and sedimentary architecture of a beach-ridge system (Anholt, the Kattegat Sea): a record of punctuated coastal progradation and sea-level change over the past similar to 1000 years. Boreas 41 (3), 422–434. https://doi.org/10.1111/j.1502-3885.2012.00250.x.

CMEMS, 2021. Atlantic- European North West Shelf- Wave Physics Reanalysis Product (WAV_004_015) [in E.U. Copernicus Marine Service Information. Available at: https://resources.marine.copernicus.eu/?option=com_csw&view=details&product_id=NWSHELF_REANALYSIS_WAV_004_015 (Accessed:CMEMS 20/02/2021).

Cuttler, M.V.W., Vos, K., Branson, P., Hansen, J.E., O'Leary, M., Browne, N.K., Lowe, R. J., 2020. Interannual response of reef islands to climate-driven variations in water level and wave climate. Remote Sens. 12 (24) https://doi.org/10.3390/rs12244089.

Dai, C., Howat, I.M., Larour, E., Husby, E., 2019. Coastline extraction from repeat high resolution satellite imagery. Remote Sens. Environ. 229, 260–270. https://doi.org/10.1016/j.rse.2019.04.010.

D'Anna, M., Idier, D., Castelle, B., Vitousek, S., Le Cozannet, G., 2021. Reinterpreting the Bruun Rule in the context of equilibrium shoreline models. J. Mar. Sci. Eng. 9 (9), 22. https://doi.org/10.3390/jmse9090974.

Dhu, T., Dunn, B., Lewis, B., Lymburner, L., Mueller, N., Telfer, E., Lewis, A., McIntyre, A., Minchin, S., Phillips, C., 2017. Digital earth Australia – unlocking new value from earth observation data. Big Earth Data 1 (1–2), 64–74. https://doi.org/10.1080/20964471.2017.1402490.

Dodet, G., Castelle, B., Masselink, G., Scott, T., Davidson, M., Floc'h, F., Jackson, D., Suanez, S., 2019. Beach recovery from extreme storm activity during the 2013–14 winter along the Atlantic coast of Europe. Earth Surf. Process. Landf. 44 (1), 393–401. https://doi.org/10.1002/esp.4500.

Dolan, R., Fenster, M.S., Holme, S.J., 1991. Temporal analysis of shoreline recession and accretion. J. Coast. Res. 723–744.

Farris, A.S., List, J.H., 2007. Shoreline change as a proxy for subaerial beach volume change. J. Coast. Res. 23 (3), 740–748. https://doi.org/10.2112/05-0442.1.

Fisher, A., Flood, N., Danaher, T., 2016. Comparing Landsat water index methods for automated water classification in eastern Australia. Remote Sens. Environ. 175, 167–182. https://doi.org/10.1016/j.rse.2015.12.055.

Flemming, B.W., 2011. 3.02 - Geology, Morphology, and Sedimentology of Estuaries and Coasts. In: Wolanski, E., McLusky, D. (Eds.), Treatise on Estuarine and Coastal Science. Academic Press, Waltham, pp. 7–38.

Garcia-Rubio, G., Huntley, D., Russell, P., 2015. Evaluating shoreline identification using optical satellite images. Mar. Geol. 359, 96–105. https://doi.org/10.1016/j.margeo.2014.11.002.

Gorelick, N., Hancher, M., Dixon, M., Ilyushchenko, S., Thau, D., Moore, R., 2017. Google Earth Engine: planetary-scale geospatial analysis for everyone. Remote Sens. Environ. 202, 18–27. https://doi.org/10.1016/j.rse.2017.06.031.

Hagenaars, G., de Vries, S., Luijendijk, A.P., de Boer, W.P., Reniers, A.J.H.M., 2018. On the accuracy of automated shoreline detection derived from satellite imagery: a case study of the sand motor mega-scale nourishment. Coast. Eng. 133, 113–125. https://doi.org/10.1016/j.coastaleng.2017.12.011.

Harley, M.D., Turner, I.L., Kinsela, M.A., Middleton, J.H., Mumford, P.J., Splinter, K.D., Phillips, M.S., Simmons, J.A., Hanslow, D.J., Short, A.D., 2017. Extreme coastal erosion enhanced by anomalous extratropical storm wave direction. Sci. Rep. 7 (1), 6033. https://doi.org/10.1038/s41598-017-05792-1.

Harley, M.D., Masselink, G., Ruiz de Alegría-Arzaburu, A., Valiente, N.G., Scott, T., 2022. Single extreme storm sequence can offset decades of shoreline retreat projected to result from sea-level rise. Commun. Earth & Environ. 3 (1), 112. https://doi.org/10.1038/s43247-022-00437-2.

Heimhuber, V., Vos, K., Fu, W., Glamore, W., 2021. InletTracker: an open-source Python toolkit for historic and near real-time monitoring of coastal inlets from Landsat and Sentinel-2. Geomorphology 389, 107830. https://doi.org/10.1016/j.geomorph.2021.107830.

Hein, C.J., Fallon, A.R., Rosen, P., Hoagland, P., Georgiou, I.Y., FitzGerald, D.M., Morris, M., Baker, S., Marino, G.B., Fitzsimons, G., 2019. Shoreline Dynamics along a developed River Mouth Barrier Island: multi-decadal cycles of erosion and event-driven mitigation. Front. Earth Sci. 7 (103) https://doi.org/10.3389/feart.2019.00103.

Konlechner, T.M., Kennedy, D.M., O'Grady, J.J., Leach, C., Ranasinghe, R., Carvalho, R. C., Luijendijk, A.P., McInnes, K.L., Ierodiaconou, D., 2020. Mapping spatial variability in shoreline change hotspots from satellite data; a case study in Southeast Australia. Estuar. Coast. Shelf Sci. 246, 12. https://doi.org/10.1016/j.ecss.2020.107018.

Kuleli, T., Guneroglu, A., Karsli, F., Dihkan, M., 2011. Automatic detection of shoreline change on coastal Ramsar wetlands of Turkey. Ocean Eng. 38 (10), 1141–1149. https://doi.org/10.1016/j.oceaneng.2011.05.006.

Kumar, D., Takewaka, S., 2019. Automatic shoreline position and intertidal foreshore slope detection from X-band radar images using modified temporal waterline method with corrected wave run-up. J. Mar. Sci. Eng. 7 (2), 28. https://doi.org/10.3390/jmse7020045.

Languille, F., Dechoz, C., Gaudel, A., Greslou, D., de Lussy, F., Tremas, T., Poulain, V., 2015. Sentinel 2 Geometric image quality commissioning - first results. In: Conference on image and Signal Processing for Remote Sensing XXI. Toulouse, FRANCE Sep 21-23. Spie-Int Soc Optical Engineering.

Lemos, C., Floc'h, F., Yates, M., Le Dantec, N., Marieu, V., Hamon, K., Cuq, V., Suanez, S., Delacourt, C., 2018. Equilibrium modeling of the beach profile on a macrotidal embayed low tide terrace beach. Ocean Dyn. 68 (9), 1207–1220. https://doi.org/10.1007/s10236-018-1185-1.

Liu, Q., Trinder, J., Turner, I., 2017. Automatic super-resolution shoreline change monitoring using Landsat archival data: a case study at Narrabeen–Collaroy Beach, Australia. J. Appl. Remote. Sens. 11 (1), 016036. https://doi.org/10.1117/1.JRS.11.016036.

Longuet-Higgins, M.S., Stewart, R.w., 1964. Radiation stresses in water waves; a physical discussion, with applications. Deep-Sea Res. Oceanogr. Abstr. 11 (4), 529–562. https://doi.org/10.1016/0011-7471(64)90001-4.

Luijendijk, A., Hagenaars, G., Ranasinghe, R., Baart, F., Donchyts, G., Aarninkhof, S., 2018. The state of the world's beaches. Sci. Rep. 8 (1), 1–11. https://doi.org/10.1038/s41598-018-28915-8.

Maraldi, C., Chanut, J., Levier, B., Ayoub, N., De Mey, P., Reffray, G., Lyard, F., Cailleau, S., Drevillon, M., Fanjul, E.A., Sotillo, M.G., Marsaleix, P., Mercator Res Dev, T., 2013. NEMO on the shelf: assessment of the Iberia-Biscay-Ireland configuration. Ocean Sci. 9 (4), 745–771. https://doi.org/10.5194/os-9-745-2013.

McAllister, E., Payo, A., Novellino, A., Dolphin, T., Medina-Lopez, E., 2022. Multispectral satellite imagery and machine learning for the extraction of shoreline indicators. Coast. Eng. 174, 104102. https://doi.org/10.1016/j.coastaleng.2022.104102.

McCarroll, R.J., Masselink, G., Valiente, N.G., Scott, T., Wiggins, M., Kirby, J.A., Davidson, M., 2021. A rules-based shoreface translation and sediment budgeting tool for estimating coastal change: ShoreTrans. Mar. Geol. 435, 27. https://doi.org/10.1016/j.margeo.2021.106466.

Mentaschi, L., Vousdoukas, M.I., Pekel, J.-F., Voukouvalas, E., Feyen, L., 2018. Global long-term observations of coastal erosion and accretion. Sci. Rep. 8 (1) https://doi.org/10.1038/s41598-018-30904-w.

Montano, J., Coco, G., Chataigner, T., Yates, M., Le Dantec, N., Suanez, S., Cagigal, L., Floc'h, F., Townend, I., 2021. Time-scales of a Dune-Beach system and implications for shoreline modeling. J. Geophys. Res. Earth Surf. 126 (11), 24. https://doi.org/10.1029/2021jf006169.

Mortlock, T.R., Goodwin, I.D., 2015. Directional wave climate and power variability along the Southeast Australian shelf. Cont. Shelf Res. 98, 36–53. https://doi.org/10.1016/j.csr.2015.02.007.

Nicholls, R.J., Wong, P.P., Burkett, V., Codignotto, J., Hay, J., McLean, R., Ragoonaden, S., Woodroffe, C.D., Abuodha, P., Arblaster, J., 2007. Coastal Systems and Low-Lying Areas.

Palomar-Vázquez, J., Almonacid-Caballer, J., Pardo-Pascual, J., Sanchez-García, E., 2018. SHOREX: a new tool for automatic and massive extraction of shorelines from Landsat and Sentinel 2 imagery. In: 7th International Conference on the Application of Physical Modelling in Coastal and Port Engineering and Science (Coastlab). Santander.

Pardo-Pascual, J.E., Almonacid-Caballer, J., Ruiz, L.A., Palomar-Vázquez, J., 2012. Automatic extraction of shorelines from Landsat TM and ETM+ multi-temporal images with subpixel precision. Remote Sens. Environ. 123, 1–11. https://doi.org/10.1016/j.rse.2012.02.024.

Pardo-Pascual, J.E., Sánchez-García, E., Almonacid-Caballer, J., Palomar-Vázquez, J.M., Priego de los Santos, E., Fernández-Sarría, A., Balaguer-Beser, Á., 2018. Assessing the accuracy of automatically extracted shorelines on microtidal beaches from landsat 7, landsat 8 and sentinel-2 imagery. Remote Sens. 10 (2), 326. https://doi.org/10.3390/rs10020326.

Pfeffer, J., Cazenave, A., Barnoud, A., 2021. Analysis of the interannual variability in satellite gravity solutions: detection of climate modes fingerprints in water mass displacements across continents and oceans. Clim. Dyn. 20. https://doi.org/10.1007/s00382-021-05953-z.

Poate, T.G., McCall, R.T., Masselink, G., 2016. A new parameterisation for runup on gravel beaches. Coast. Eng. 117, 176–190. https://doi.org/10.1016/j.coastaleng.2016.08.003.

Robinet, A., Castelle, B., Idier, D., Le Cozannet, G., Déqué, M., Charles, E., 2016. Statistical modeling of interannual shoreline change driven by North Atlantic climate variability spanning 2000–2014 in the Bay of Biscay. Geo-Mar. Lett. 36 (6), 479–490. https://doi.org/10.1007/s00367-016-0460-8.

Ruessink, B.G., Kleinhans, M.G., Van Den Beukel, P.G.L., 1998. Observations of swash under highly dissipative conditions. J. Geophys. Res. Oceans 103 (C2), 3111–3118. https://doi.org/10.1029/97jc02791.

Ruggiero, P., Komar, P.D., McDougal, W.G., Marra, J.J., Beach, R.A., 2001. Wave runup, extreme water levels and the erosion of properties backing beaches. J. Coast. Res. 17 (2), 407–419.

Sánchez-García, E., Palomar-Vázquez, J.M., Pardo-Pascual, J.E., Almonacid-Caballer, J., Cabezas-Rabadán, C., Gómez-Pujol, L., 2020. An efficient protocol for accurate and massive shoreline definition from mid-resolution satellite imagery. Coast. Eng. (Amsterdam) 160, 103732. https://doi.org/10.1016/j.coastaleng.2020.103732.

Sayre, R., Noble, S., Hamann, S., Smith, R., Wright, D., Breyer, S., Butler, K., Van Graafeiland, K., Frye, C., Karagulle, D., Hopkins, D., Stephens, D., Kelly, K., Basher, Z., Burton, D., Cress, J., Atkins, K., Van Sistine, D.P., Friesen, B., Allee, R., Allen, T., Aniello, P., Asaad, I., Costello, M.J., Goodin, K., Harris, P., Kavanaugh, M., Lillis, H., Manca, E., Muller-Karger, F., Nyberg, B., Parsons, R., Saarinen, J., Steiner, J., Reed, A., 2019. A new 30 meter resolution global shoreline vector and associated global islands database for the development of standardized ecological coastal units. J. Operat. Oceanogr. 12 (sup2), S47–S56. https://doi.org/10.1080/1755876X.2018.1529714.

Senechal, N., Coco, G., Bryan, K.R., Holman, R.A., 2011. Wave runup during extreme storm conditions. J. Geophys. Res. 116 (C7) https://doi.org/10.1029/2010jc006819.

Smith, R.K., Bryan, K.R., 2007. Monitoring Beach Face volume with a combination of intermittent profiling and video imagery. J. Coast. Res. 23 (4), 892–898. https://doi.org/10.2112/04-0287.1.

Sorensen, R.M., 2006. Basic Coastal Engineering, 3rd edn. Springer Science+Business Media, New York: New York.

Splinter, K.D., Turner, I.L., Davidson, M.A., Barnard, P., Castelle, B., Oltman-Shay, J., 2014. A generalized equilibriummodel for predicting daily to interannual shoreline response. J. Geophys. Res. Earth Surf. 119 (9), 1936–1958. https://doi.org/10.1002/2014jf003106.

Stammer, D., Ray, R.D., Andersen, O.B., Arbic, B.K., Bosch, W., Carrere, L., Cheng, Y., Chinn, D.S., Dushaw, B.D., Egbert, G.D., Erofeeva, S.Y., Fok, H.S., Green, J.A.M., Griffiths, S., King, M.A., Lapin, V., Lemoine, F.G., Luthcke, S.B., Lyard, F., Morison, J., Muller, M., Padman, L., Richman, J.G., Shriver, J.F., Shum, C.K., Taguchi, E., Yi, Y., 2014. Accuracy assessment of global barotropic ocean tide models. Rev. Geophys. 52 (3), 243–282. https://doi.org/10.1002/2014rg000450.

Stive, M.J.F., Aarninkhof, S.G.J., Hamm, L., Hanson, H., Larson, M., Wijnberg, K.M., Nicholls, R.J., Capobianco, M., 2002. Variability of shore and shoreline evolution. Coast. Eng. 47 (2), 211–235. https://doi.org/10.1016/s0378-3839(02)00126-6.

Stockdon, H.F., Holman, R.A., Howd, P.A., Sallenger, A.H., 2006. Empirical parameterization of setup, swash, and runup. Coast. Eng. 53 (7), 573–588. https://doi.org/10.1016/j.coastaleng.2005.12.005.

Stokes, K., Poate, T., Masselink, G., King, E., Saulter, A., Ely, N., 2021. Forecasting coastal overtopping at engineered and naturally defended coastlines. Coast. Eng. (Amsterdam) 164. https://doi.org/10.1016/j.coastaleng.2020.103827.

Storey, J., Choate, M., Lee, K., 2014. Landsat 8 Operational Land Imager On-Orbit Geometric Calibration and Performance. Remote Sens. 6 (11), 11127–11152. https://doi.org/10.3390/rs61111127.

Sudmanns, M., Tiede, D., Augustin, H., Lang, S., 2020. Assessing global Sentinel-2 coverage dynamics and data availability for operational Earth observation (EO) applications using the EO-Compass. Int. J. Dig. Earth 13 (7), 768–784. https://doi.org/10.1080/17538947.2019.1572799.

Tonani, A., Saulter, A., 2020. NWSHELF_REANALYSIS_WAV_004_015 Product User Manual (PUM), 1.0 edn. EU: Copernicus Marine Service Information. Available at: https://catalogue.marine.copernicus.eu/documents/PUM/CMEMS-NWS-PUM-004-015.pdf. (Accessed: 14/08/2021).

Turner, I.L., Harley, M.D., Short, A.D., Simmons, J.A., Bracs, M.A., Phillips, M.S., Splinter, K.D., 2016. A multi-decade dataset of monthly beach profile surveys and inshore wave forcing at Narrabeen, Australia. Sci. Data 3, 13. https://doi.org/10.1038/sdata.2016.24.

Turner, I.L., Harley, M.D., Almar, R., Bergsma, E.W.J., 2021. Satellite optical imagery in Coastal Engineering. Coast. Eng. 167, 8. https://doi.org/10.1016/j.coastaleng.2021.103919.

Valiente, N.G., McCarroll, R.J., Masselink, G., Scott, T., Wiggins, M., 2019. Multi-annual embayment sediment dynamics involving headland bypassing and sediment exchange across the depth of closure. Geomorphology 343, 48–64. https://doi.org/10.1016/j.geomorph.2019.06.020.

Vitousek, S., Barnard, P.L., Limber, P., 2017. Can beaches survive climate change? J. Geophys. Res. Earth Surf. 122 (4), 1060–1067. https://doi.org/10.1002/2017jf004308.

Vos, K., Harley, M.D., Splinter, K.D., Simmons, J.A., Turner, I.L., 2019a. Sub-annual to multi-decadal shoreline variability from publicly available satellite imagery. Coast. Eng. 150, 160–174. https://doi.org/10.1016/j.coastaleng.2019.04.004.

Vos, K., Splinter, K.D., Harley, M.D., Simmons, J.A., Turner, I.L., 2019b. CoastSat: a Google Earth Engine-enabled Python toolkit to extract shorelines from publicly available satellite imagery. Environ. Model. Softw. 122, 7. https://doi.org/10.1016/j.envsoft.2019.104528.

Vos, K., Harley, M.D., Splinter, K.D., Walker, A., Turner, I.L., 2020. Beach slopes from satellite-derived shorelines. Geophys. Res. Lett. 47 (14), 10. https://doi.org/10.1029/2020gl088365.

Vos, K., Harley, M., Turner, I., Splinter, K., 2021a. Large Regional Variability in Coastal Erosion Caused by ENSO.

Vos, K., Harley, M., Turner, I., Splinter, K., . Large Regional Variability in Coastal Erosion Caused by ENSO. https://assets.researchsquare.com/. Preprint. https://doi.org/10.21203/rs.3.rs-666160/v1.

Wiggins, M., Scott, T., Masselink, G., Russell, P., McCarroll, R.J., 2019a. Coastal embayment rotation: Response to extreme events and climate control, using full embayment surveys. Geomorphology 327, 385–403. https://doi.org/10.1016/j.geomorph.2018.11.014.

Wiggins, M., Scott, T., Masselink, G., Russell, P., Valiente, N.G., 2019b. Regionally-coherent embayment rotation: behavioural response to bi-directional waves and atmospheric forcing. J. Mar. Sci. Eng. 7 (4), 18. https://doi.org/10.3390/jmse7040116.

Wiggins, M., Scott, T., Masselink, G., McCarroll, R.J., Russell, P., 2020. Predicting beach rotation using multiple atmospheric indices. Mar. Geol. 426, 106207. https://doi.org/10.1016/j.margeo.2020.106207.

Wulder, M.A., White, J.C., Loveland, T.R., Woodcock, C.E., Belward, A.S., Cohen, W.B., Fosnight, E.A., Shaw, J., Masek, J.G., Roy, D.P., 2016. The global Landsat archive: Status, consolidation, and direction. Remote Sens. Environ. 185, 271–283. https://doi.org/10.1016/j.rse.2015.11.032.

Yates, M., Guza, R., O'Reilly, W., Hansen, J., Barnard, P., 2011. Equilibrium shoreline response of a high wave energy beach. J. Geophys. Res. Oceans 116 (C4).

Young, N.E., Anderson, R.S., Chignell, S.M., Vorster, A.G., Lawrence, R., Evangelista, P. H., 2017. A survival guide to Landsat preprocessing. Ecology 98 (4), 920–932. https://doi.org/10.1002/ecy.1730.

Zaron, E.D., Elipot, S., 2021. An assessment of global ocean barotropic tide models using geodetic mission altimetry and surface drifters. J. Phys. Oceanogr. 51 (1), 63–82. https://doi.org/10.1175/JPO-D-20-0089.1.